



Royal Academy
of Engineering

Power-to-X for a Sustainable Future Workshop 2025 in association with ASSSI

PROCEEDINGS

September 15th, 2025
Montien Hotel Surawong, Bangkok, Thailand



<https://www.thaienergystorage.org/power-to-x-for-a-sustainable-future-work>

PROCEEDINGS

**Power-to-X for a Sustainable Future Workshop 2025
September 15, 2025**

**at
Montien Hotel Surawong, Bangkok, Thailand**

**Organized by
Assoc. Prof. Soorathep Kheawhom
Dr. Chanon Pornrungsroj**

**In association with
The Department of Chemical Engineering, Faculty of Engineering,
Chulalongkorn University**

POWER-TO-X FOR SUSTAINABLE FUTURE WORKSHOP 2025

First published: January 2026

National Library of Thailand Cataloging in Publication Data

ISBN (e-book): 978-616-621-082-8

Advisor Dr. Watcharaphol Paritmongkol

 Prof. Dr.Patchanita Thamyongkit

 Prof. Dr. Benjapon Chalermssinsuwan

 Asst. Prof. dr. Junjuda Unruangsri

 Asst.Prof. Motiar Rahaman

Organizing Committee Assoc. Prof. Dr. Soorathep Kheawhom

 Dr. Chanon Pornrungroj

Published by Chulalongkorn University

 254 Phayathai Road, Wang Mai, Pathumwan, Bangkok 10330, Thailand



Message from the Chairperson



Welcome to the *Power-to-X for a Sustainable Future Workshop 2025*, taking place on 15 September 2025 at the Montien Hotel Surawong in Bangkok, in association with ASSSI.

Power-to-X has become a practical way to connect renewable electricity with real needs in society, from clean hydrogen and sustainable chemicals to long-duration storage and grid flexibility. Progress, however, does not come from one discipline alone. It depends on materials, electrochemistry, catalysis, system design, and deployment working together. That is why I am especially glad to see researchers and practitioners from many backgrounds joining this workshop.

Our program is designed to encourage both learning and honest discussion. The invited talks, parallel sessions, and posters cover a wide range of topics, highlighting new results while also pointing to what still limits performance, durability, and scale-up. I hope the conversations here help clarify priorities, spark new ideas, and build collaborations that continue after the workshop ends.

My sincere thanks go to all speakers, session chairs, committee members, and supporters who made this event possible. I also thank every participant for being here and for contributing your time and expertise.

I wish you an engaging and productive workshop, and I look forward to the discussions and connections that will come from it.

Assoc. Prof. Dr. Soorathep Kheawhom

Chairperson, Power-to-X for a Sustainable Future Workshop 2025

Faculty of Engineering, Chulalongkorn University



Committee





Scientific Committee

1. Dr. Watcharaphol Paritmongkol

Vidyasirimedhi Institute of Science and Technology (VISTEC)

2. Prof. Dr. Patchanita Thamyongkit

Faculty of Science Chulalongkorn University

3. Prof. Dr. Benjapon Chalermnsinsuwan

Faculty of Science Chulalongkorn University

4. Asst. Prof. dr. Junjuda Unruangsri

Faculty of Science Chulalongkorn University

5. Asst. Prof. Motiar Rahaman

Academic Chair in Power-to-Fuel at University of Liège, Belgium.

Local Organizing Committee

1. Assoc. Prof. Dr. Soorathep Kheawhom

Faculty of Engineering Chulalongkorn University

2. Associate Professor Lapyote Prasittisopin

Faculty of Science Chulalongkorn University

3. Dr. Orapa Tamwattana

Faculty of Science Khon Kaen University

4. Dr. Chanon Pornrungrroj

Faculty of Engineering Chulalongkorn University





5. Assoc. Prof Dr. Rojana Pornprasertsuk

Faculty of Science Chulalongkorn University

6. Assist. Prof. Dr. Prasit Pattanauwat

Faculty of Science Chulalongkorn University

7. Dr. Manunya Okhawilai

Faculty of Engineering Chulalongkorn University

8. Prof. Dr. Anongnat Somwangthanaroj

Faculty of Engineering Chulalongkorn University

9. Dr. Jiaqian Qin

Faculty of Science Chulalongkorn University

10. Dr. Wanwisa Limphirat

Synchrotron Light Research Institute, SLRI





Power-to-X

for a Sustainable Future
Workshop 2025
15 September 2025



Workshop Program





Power-to-X (P2X) Workshop Program

Day#0 : Sunday 14 September 2025

(Bangkok, Thailand)

Time	Programme
17.00 – 20.00	Welcome reception for ASSSI Board members @ Mandarin Hotel Lobby





Day#1 : Monday 15 September 2025
(Montien Hotel, Surawong, Bangkok, Thailand)

Time	Programme
Location: An-an Meeting Room	
08.30 – 09.00	Registration
09.00 – 09.20	<ul style="list-style-type: none">• Welcome Remarks by Assoc. Prof. Dr. Soorathep Kheawhom,• Opening Remarks by Assoc. Prof. Dr. Wittaya Wannasuphprasit, Dean, Faculty of Engineering, Chulalongkorn University• Photo Session
09.20 – 10.00	Coffee Break





Session#A @ An-an#1		Session#B @ An-an #2	
Chair: Assoc. Prof. Dr. Rojana Pornprasertsuk Co-Chair: Dr. Manunya Okhawilai Co-Chair: Prof. Dr. Anongnat Somwangthanaroj		Chair: Asst. Prof. Dr. Junjuda Unruangsri Co-Chair: Dr. Panawan Vanaphuti	
10.00 – 10.20	Invited#A1 (University of Texas at Dallas, USA) – Asst. Prof. Dr. Laisuo Su <online> <i>Sodium Halide Solid State Electrolyte with High Ionic Conductivity</i>	10.00 – 10.20	Invited#B1 (VISTEC, Thailand) – Assoc. Prof. Dr. Chularat Wattanakit <i>Asymmetric Synthesis of Chiral Compounds from CO₂ at Chiral Encoded Metal Surfaces</i>
10.20 – 10.40	Invited#A2 (Central South University, China) – Prof. Dr. Yue Yang <online> <i>Recycling and Material Regeneration of Spent Lithium-ion Battery Materials</i>	10.20 – 10.40	Invited#B2 (NANOTEC, Thailand) – Dr. Pongkarn Chakthranont <i>Electrochemical Systems for CO₂ Utilization and Biomass Valorization</i>
10.40 – 11.00	Invited#A3 (Thammasat University, Thailand) – Prof. Dr. Nurak Grisdanurak <i>Pilot Scale Study for Precious Metals from LIB waste</i>	10.40 – 11.00	Invited#B3 (Indian Institute of Technology Kanpur, India) – Prof. Raju Kumar Gupta <i>Pore-Engineered Carbon from Sugarcane Bagasse for Sodium-Ion Battery and CO₂ Capture Applications</i>
11.00 – 11.20	Invited#A4 (Institut Teknologi Sepuluh Nopember, Indonesia) – Prof. Dr. Lukman Noerochim <online> <i>Low-Energy Direct Regeneration Methods for Spent Cathode Materials in Lithium-Ion Batteries</i>	11.00 – 11.20	Invited#B4 (Sirindhorn International Institute of Technology, Thailand) – Asst. Prof. Dr. Pawin Iamprasertkun <i>Sustainable Electrochemical Intelligence for 2D Materials</i>



11.20 – 11.40	Invited#A5 (Kogakuin University, Japan) – Prof. Dr. Takuya Okazaki <online> <i>Hydrothermal Selective Leaching of Lithium from LiCoO₂ under CO₂ Atmosphere</i>	11.20 – 11.40	Invited#B5 (China Three Georges University, China) – Prof. Dr. Xuelin Yang <i>Carbon Materials: Multiscale Structure Regulation and Applications in Electrochemical Energy Storage</i>
11.40 – 12.00	Invited#A6 (Indian Institute of Science Education and Research Tirupati, India) – Dr. Vanchiappan Aravindan <i>Transforming Spent Li-ion Battery Graphite into High-Performance Hybrid Cathodes</i>	11.40 – 12.00	Invited#B6 (Sookmyung Women's University, South Korea) – Prof. Dr. Won-Hee Ryu <i>Designing Electrolyte Additives for Stable and Fast Charging Alkali Metal Batteries</i>
12.00 – 13.30	Lunch @		
Session#C @ An-an #1 Chair: Dr. Chanon Pomrungrroj Co-Chair: Assoc. Prof. Dr. Lapyote Prasittisopin		Session#D @ An-an #2 Chair: Assoc. Prof. Dr. Soorathep Kheawhom Co-Chair: Asst. Prof. Dr. Prasit Pattananuwat Co-Chair: Dr. Jiaqian Qin	
13.30 – 13.50	Invited#C1 (University of Liège, Belgium) – Dr. Motiar Rahaman <online> <i>Sunlight-to-Chemicals: A Robust Biohybrid System for Formic Acid Production</i>	13.30 – 13.50	Invited#D1 (Tianjin University, China) – Prof. Dr. Quan-Hong Yang <i>“Sieving” Means “Energetic”: Carbon Design for High-Energy Sodium Batteries</i>





13.50 – 14.10	Invited#C2 (Indian Institute of Technology Roorkee, India) – Prof. Dr. Monojit Bag <i>Bi-functional Halide Perovskite-based Electrodes for Photo-rechargeable Supercapacitor: Application in Off-grid Energy Sectors</i>	13.50 – 14.10	Invited#D2 (Sejong University, South Korea) – Prof. Dr. Seung-Taek Myung <i>Mn-rich layered cathode materials for lithium and sodium intercalation</i>
14.10 – 14.30	Invited#C3 (Shinshu University, Japan) – Asst. Prof. Dr. Mongkol Tipplook <i>Investigation of Sodium Manganese Oxides with Various Crystal Phases as Sodium Ion battery Cathode Materials</i>	14.10 – 14.30	Invited#D3 (A*STAR Institute of Materials Research and Engineering, Singapore) – Adj. Asst. Prof. Dr. Derrick W. H. Fam <i>Dynamically crosslinked polymer electrolytes for all solid state batteries</i>
14.30 – 14.50	Invited#C4 (Materials Research Centre, Coimbatore, India) – Prof. Dr. S. Selvasekarapandian <i>Bio-materials as Electrolyte for Electrochemical Devices</i>	14.30 – 14.50	Invited#D4 (Institute of Physics, CAS, China) – Prof. Dr. Hong Li <i>Practical solid batteries via in situ solidification technologies</i>
14.50 – 15.10	Invited#C5 (Khon Kaen University, Thailand) – Dr. Orapa Tamwattana <i>Synergistic LiF@PVDF–MOF Interface for Long-Life Anode-Free Lithium-Metal Batteries</i>	14.50 – 15.10	Invited#D5 (National University of Singapore, Singapore) – Assoc. Prof. Dr. Stefan Adams <i>Compressible Light Solid Electrolytes for Durable High Energy Solid-State Batteries</i>



15.10 – 15.30	Invited#C6 (University of Petroleum and Energy Studies, India) – Mr. Rajkamal Arya <i>Redox Dynamics of anion-Doped Cobalt hydroxide/carbon composite for High-Performance Supercapattery Applications</i>	15.10 – 15.30	Invited#D6 (Shanghai Institute of Ceramics, Chinese Academy of Science, China) – Prof. Dr. Zhaoyin Wen <i>Modification strategies for interfaces in all solid state secondary batteries</i>
15.30 – 16.00	Coffee break		
16.00 – 17.00	Poster session @ Piman Room	16.00 – 17.00	Closed Meeting for ASSSI Board members
17.30 – 21.00	Dinner – Banquet @ Ruenton <Invitation only>		





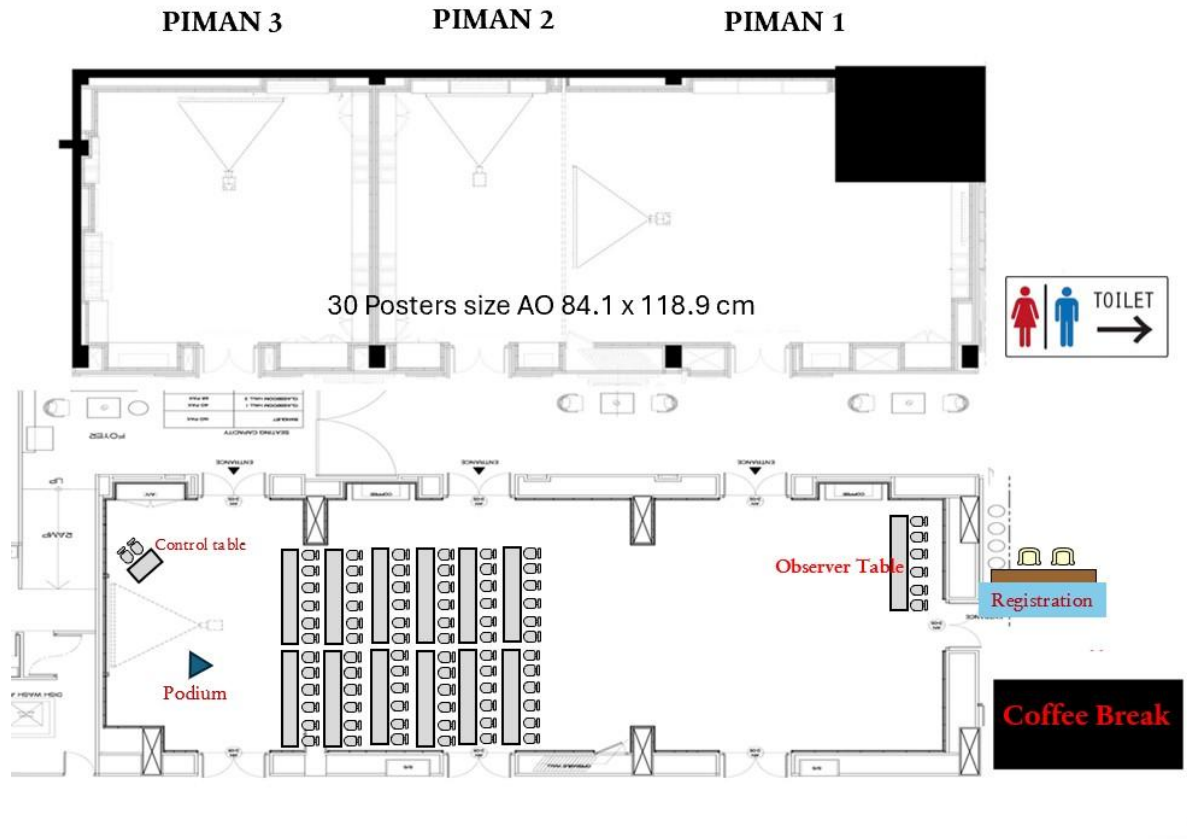
Day#2 : Tuesday 16 September 2025
(Chulalongkorn University, Bangkok, Thailand)

Time	Programme
09.00 – 12.00	Collaborative Meeting for ASSSI Board members and Organizing committees @ Suan Ruam Jai Room
12.00 – 13.30	Lunch @ Suan Ruam Jai Room
13.30 – 15.30	Lab Tour @ 100 th Anniversary Engineering Building





Layout of the conference





Outline

Message from chairperson	A
Committee	B-D
Workshop Program	E-L
Layout of the conference	M
Manuscript	
- Ligand-Engineered Cobalt MOFs with Bipyridine for Efficient OER	2-14
- Functionalized Halloysite Nanotube filled Poly (Vinyl Alcohol)/ Quaternized Chitosan as Bio-based Composite Polymer Membrane for Alkaline Electrolysis	15-29
- Improving Coulombic Efficiency in Anthraquinone–Bromine Flow Batteries with an Aqueous Bromine Complexant	30-41
- Bio-Based Quasi Solid Polymer Electrolytes for High Performance Zinc-Ion Batteries	42-54



POWER-TO-X FOR A SUSTAINABLE FUTURE WORKSHOP 2025

in association with ASSSI

15th September 2025

AT MONTIEN HOTEL SURAWONG, BANGKOK, THAILAND.

○○○○

*A board meeting of the Asian Society for Solid State Ionics (ASSSI) will be held in conjunction with this event.

*A board meeting of the Asian Society for Solid State Ionics (ASSSI) will be held in conjunction with this event.

Supported by



Royal Academy
of Engineering



Power-to-X

for a Sustainable Future

Workshop 2025

15 September 2025



MANUSCRIPT





Ligand-Engineered Cobalt MOFs with Bipyridine for Efficient OER

Muzammil Shah¹, Mohan Gopalakrishnan¹ and Soorathep Kheawhom^{1,2*},

¹*Department of Chemical Engineering, Faculty of Engineering, Chulalongkorn University, Bangkok 10330*

²*Center of Excellence on Advanced Materials for Energy Storage, Chulalongkorn University, Bangkok 10330, Thailand*

**Corresponding author's e-mail address: Soorathep.k@chula.ac.th*

Abstract

Water electrolysis offers a clean pathway to hydrogen in a carbon-neutral energy system, yet the oxygen evolution reaction (OER) remains the kinetic bottleneck and demands efficient, durable electrocatalysts. Here, cobalt-based metal–organic frameworks (MOFs) were synthesized using 1,3,5-benzenetricarboxylic acid (BTC) as the linker and subsequently modified with the nitrogen-rich ligand 2,2'-bipyridine (bpy) via a simple hydrothermal route. Pyrolysis of the resulting materials produced cobalt-containing phases (cobalt element/cobalt oxide Co/Co–O) supported on a conductive carbon matrix. Structural and morphological analyses by X-ray diffraction (XRD) and scanning electron microscopy (SEM) confirmed successful framework formation and bipyridine-induced modification. Electrochemical testing in alkaline media showed that the bpy-modified MOF outperforms its BTC-only counterpart for OER, delivering higher current density at a lower onset potential. The enhancement is attributed to improved charge-transfer kinetics and a greater density of accessible active sites arising from nitrogen incorporation. These results underscore rational ligand engineering as a viable strategy for advancing MOF-derived, binder-free OER electrocatalysts.

1. Introduction

The transition to a carbon-neutral energy system requires efficient and scalable routes for renewable hydrogen production. Among current options, water electrolysis has attracted sustained attention because it delivers high-purity hydrogen without greenhouse-gas emissions [1, 2]. The overall efficiency, however, is constrained by the oxygen evolution reaction (OER)—a sluggish four-electron process that demands substantial overpotential [3, 4]. Developing robust, low-cost electrocatalysts that accelerate OER kinetics therefore remains a central objective.

Cobalt-based materials are compelling alternatives to noble-metal catalysts such as ruthenium oxide (RuO_2) and iridium oxide (IrO_2) [5, 6]. Metal–organic frameworks (MOFs) provide an attractive platform for catalyst design because their coordination environments, porosity, and topology can be tuned with precision [7, 8]. Upon pyrolysis, MOFs transform into porous metal-oxide/carbon composites that expose abundant active sites and facilitate mass and charge transport [9–11]. Despite these advantages, practical limitations persist: charge-transfer resistance often elevates OER overpotentials, and the cobalt coordination microenvironment is not easily controlled using simple, scalable synthetic handles, both of which can suppress activity and stability in alkaline media.

Ligand engineering offers a direct means to address these limitations by modulating the electronic structure and local geometry of MOF nodes [12]. Incorporating nitrogen-containing ligands such as 2,2'-bipyridine (bpy) can enhance the physicochemical properties of MOF-derived catalysts [13]; nitrogen increases electronic conductivity in the carbon matrix [14] and adjusts cobalt coordination to facilitate charge transfer while stabilizing reaction intermediates [15]. Yet, the deliberate introduction of a chelating N-ligand into a Co–BTC (Co = Cobalt, BTC = 1,3,5-benzene tricarboxylic acid) framework, and the resulting consequences for precursor structure, defect chemistry, and the properties of Cobalt/Cobalt oxide (Co/Co–O) phases supported on N-doped carbon after pyrolysis, have not been systematically evaluated.

Although cobalt-based MOF electrocatalysts for oxygen evolution reaction (OER) have been widely explored, most studies focus on common linker geometries and lack comparative analysis of

linker effects on catalytic performance and stability. There is a critical need for deeper insight into how rational ligand-level design can tune the structure, electronic properties, and active site accessibility in MOF-derived catalysts [16].

In this work, Co–BTC MOFs are synthesized and modified in situ with 2,2'-bipyridine via a simple hydrothermal route, then pyrolyzed to generate Co/Co–O species on a conductive N-doped carbon matrix.

The central premise is that bipyridine incorporation will retune cobalt coordination, increase defect density and surface area, and, after carbonization, produce electronically coupled active sites that reduce charge-transfer barriers and increase the density of accessible OER sites. Structural and morphological characterization (X-Ray diffraction XRD, Scanning electron microscopy SEM), complemented by thermal analysis, is used to establish the resulting structure–property relationships, and electrochemical testing in alkaline media demonstrates that the bipyridine-modified material outperforms its BTC-only analogue. Collectively, the results position ligand-level design as a practical and scalable strategy for advancing MOF-derived, OER electrocatalysts.

2. Methodology

1. Synthesis of Co–BTC MOF

Cobalt-based metal–organic frameworks (Co–BTC) were synthesized by a simple hydrothermal route using 1,3,5-benzenetricarboxylic acid (BTC) as the organic linker. Cobalt nitrate hexahydrate (2m.mol) was dissolved in 10 ml of deionized (DI) water under constant stirring, followed by addition of an 10ml ethanolic solution of 1m.mol BTC. To stabilize the mixture, 10 mL of N,N-dimethylformamide (DMF) was introduced. After 2 h of continuous stirring, the pH was adjusted to 8 using 1M NaOH. The suspension was transferred to a Teflon-lined autoclave and heated at 120 °C for 48 h. The resulting blue precipitate was collected, washed repeatedly with ethanol and DI water, and dried at 80 °C.



2. Synthesis of Co–BTC–bipyridine MOF

To examine the effect of a nitrogen-rich ligand, 2,2'-bipyridine (bpy) was incorporated during MOF formation. 2m.mol Cobalt nitrate, 1m.mol BTC, and 0.5m.mol of bpy were dissolved in a mixed solvent of 10 ml DI water, 10ml ethanol, and 10ml DMF under stirring, and the pH was adjusted to 8 using 1M NaOH. The mixture was then subjected to the same hydrothermal conditions as in Section 2.1 (120 °C, 48 h). The resulting solids were collected, washed repeatedly with ethanol and DI water, and dried as described for Co–bpy–BTC. Pink crystalline particles were obtained and stored for subsequent characterization.

3. Pyrolysis

Co–BTC and Co–bpy–BTC were pyrolyzed to obtain cobalt oxide/nitrogen-doped carbon composites (CoO/NC) and named as Co–BTC–750 and Co–bpy–BTC–750. Each precursor was heated under an inert N₂ atmosphere to 750 °C at a ramp rate of 5 °C min⁻¹ and held for 2 h. The resulting black powders were collected and stored for subsequent characterization.

4. Characterization

Powder X-ray diffraction (XRD) was used to determine crystalline structure and phase composition, and scanning electron microscopy (SEM) was employed to examine morphology. Together, these analyses assessed the structural integrity of the as-synthesized MOFs and the morphological evolution induced by bipyridine incorporation and subsequent pyrolysis.

5. Electrochemical Evaluation

Electrocatalytic OER performance was assessed in 0.1 M KOH using a conventional three-electrode setup. A glassy carbon electrode coated with the catalyst ink served as the working electrode, with a



platinum wire as the counter electrode and a Hg/HgO electrode as the reference. Linear sweep voltammetry (LSV) was used to determine overpotentials, and Tafel slopes were extracted from the polarization curves to evaluate reaction kinetics.

3. Results and Discussion

1. Morphological Characterization

Scanning electron microscopy (SEM) was used to examine surface morphology. As shown in Figure 1a, the pristine Co–BTC–750 displays well-faceted, polyhedral particles with relatively smooth surfaces and a narrow size distribution (figure 2b) with average particle size of 2.64 μm , consistent with morphologies commonly reported for BTC-based cobalt MOFs. The morphology is commonly associated with stable structural integrity but the defect sites are less common which restricts the exposure of the active sites for an efficient catalytic reaction as discussed in the literature [17].

Introducing 2,2'-bipyridine induces pronounced morphological evolution (Figure 1b). The Co–BTC–bpy–750 sample exhibits a more fragmented, porous architecture with rougher facets and irregular edges, indicative of increased defect density and greater textural complexity. These features suggest that bipyridine perturbs the native BTC coordination environment, promoting defect formation and an effectively higher surface area.

Such textural changes between Co–BTC–750 and Co–bpy–BTC–750 highlight the critical impact of organic linker engineering on electrocatalytic properties of Co-based MOFs. Studies suggested that tuning linker chemistry can modify electron density and metal ligand covalency resulting in lower overpotential [18]. The interference of 2,2'-bipyridine has caused distinct coordination geometries leading to the formation of intrinsic defects and unsaturated metal sites which provide an advantage for electrocatalysis because the defects facilitate surface roughness improving electrolyte penetration and local electronic pathways around cobalt centers and increase the exposure of catalytically cobalt active sites [19].

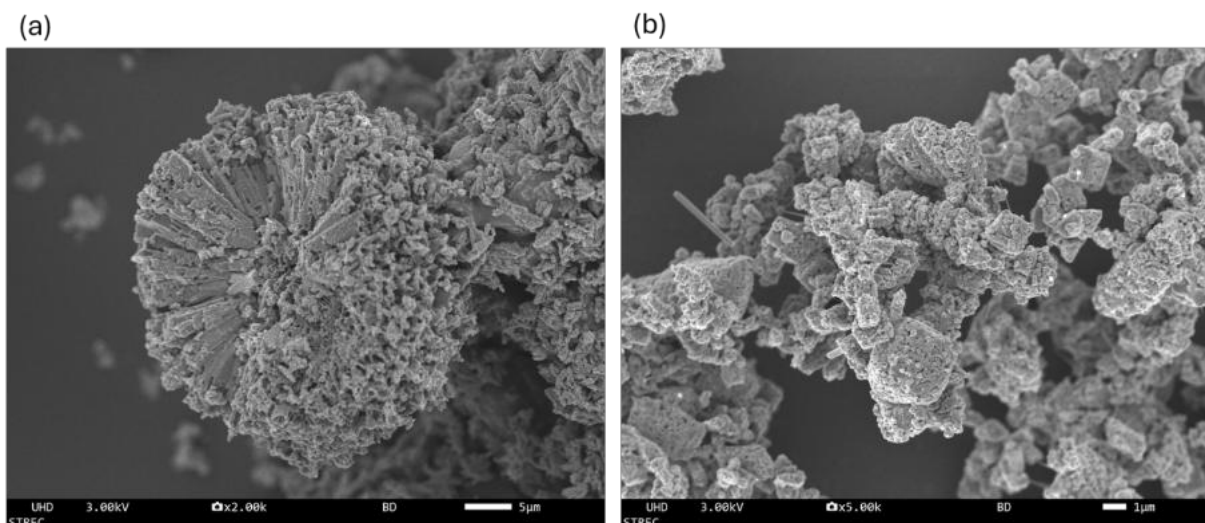


Figure 1 Scanning electron microscopy images for (a) Co-BTC-750 and (b) Co-bpy-BTC-750

2. Structural Characterization

X-ray diffraction (XRD) patterns (Figure 2a) were used to assess crystalline phases. For Co-BTC-750, distinct reflections characteristic of cobalt-containing species supported on a conductive carbon matrix are observed, with prominent peaks at 44.3° and 51.6° (2θ) indicating well-developed crystallinity in the BTC-derived catalyst consistent with previously reported works which reflect a stable framework structure and higher phase purity [20].

Upon introducing 2,2'-bipyridine leads to noticeable changes in the Co-bpy-BTC-750 pattern. The principal reflections are retained, but the intensity increases, and modest peak broadening appears consistent with partial modification of the cobalt coordination environment and the introduction of lattice disorder or microstrain. At the same time, the persistence—and in some cases higher intensity—of key reflections indicates that long-range order is maintained after bpy incorporation. The local distortions suggested the creation of defect sites which influences the electronic properties of the catalyst. This combination of preserved crystallinity with locally perturbed lattice environments can facilitate electronic transport and create catalytically favorable sites during OER [21].

The peak retention and enhancement in their intensities indicates that the framework structural integrity remains intact despite the introduction of 2,2'-bipyridine, strongly suggesting the robustness of the modified MOF and creation of defects because of missing organic linker or metal vacancies. The unsaturated metal centers serve as highly active catalytic sites which are reported as potential strategy for enhancing electrocatalytic activities [22]. The distortions can modify the electronic band structure lowering charge transfer barrier and increasing electronic conduction. The retention of long-range orders along with the defects allows smoother charge transfer and exposed cobalt active sites ensuring durability of the catalyst.

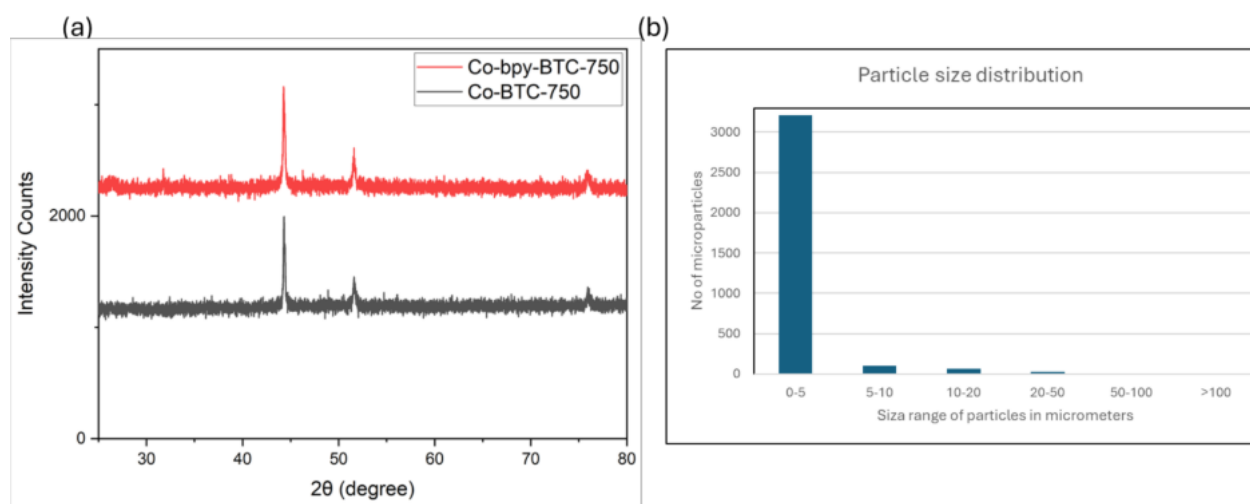


Figure 2 (a) XRD graph for confirming the conductive carbon matrix catalyst of Co-BTC-750 and Co-bpy-BTC-750 (b) particle size distribution of Co-MOF-750 particles

3. Thermal Stability Analysis

Thermal behavior was evaluated by thermogravimetric analysis (TGA) coupled with differential thermogravimetry (DTG) (Figure 3). For Co-BTC (Figure 3a), three mass-loss events are evident: an initial loss of ~15% at ~100–120 °C attributable to desorption of physisorbed water and residual solvents [23]; a second step between 300–350 °C corresponding to partial decomposition of the BTC linker; and a major degradation at ~460–520 °C ($\approx 32\%$ loss) associated with collapse of the MOF

framework and formation of cobalt oxide/alloy species. These transitions are characteristics of BTC based MOFs that are aligned with the previously reported works suggesting the structural integrity loss and formation of metal oxides and alloys at higher temperatures [24].

In comparison, Co-bpy-BTC (Figure 3b) exhibits decomposition features shifted to higher temperatures suggesting the robust nature of the catalyst. Solvent removal occurs near ~ 110 °C with minimal mass loss ($\sim 2\text{--}5\%$), indicating a strong framework interaction. The principal framework decomposition spans $400\text{--}480$ °C with a total loss of $\sim 25\text{--}30\%$ indicating enhanced thermal stability. The upward shift of the major degradation step relative to Co-BTC indicates enhanced thermal stability upon bipyridine incorporation, consistent with nitrogen-assisted stabilization of the precursor framework.

Nitrogen containing aromatic compounds strengthens the metal ligand coordination bond and promotes lattice stabilization through electron donation and additional coordination interactions. The bipyridine assisted stabilization is also verified in different MOFs [25]. The introduction of a heteroatom elevates the decomposition temperature and enhances the resistance to thermal stress. The shift in the thermal stability indicates that linker engineering has modified the thermal resistance of the MOF structure, attributing to the electrocatalyst exposure to elevated temperatures during operations or regeneration cycles. Additionally, thermal stability is also attributed to catalytic durability by preserving structural integrity and active site availability [26].

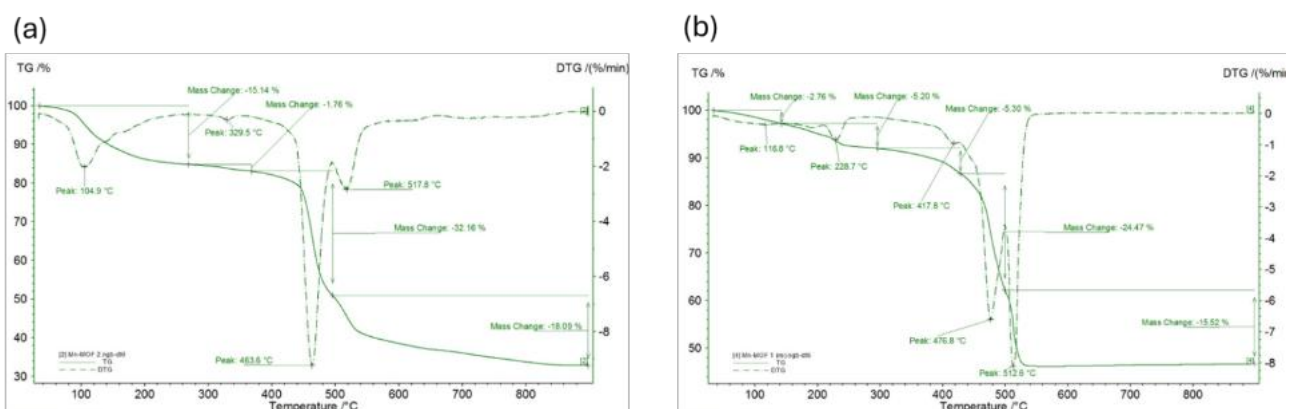


Figure 3 Thermogravimetric analysis for stability of Co-based MOFs (a) Co-BTC and (b) Co-bpy-BTC

4. Electrochemical Performance

OER activity was evaluated by linear sweep voltammetry (LSV) in 0.1M KOH (Figure 4). Both catalysts exhibit the expected anodic polarization with a sharp increase in current at higher potentials, confirming catalytic oxygen evolution. Across the potential window, Co-bpy-BTC-750 delivers higher current densities than Co-BTC-750; at 1.8 V vs RHE, the current density reaches $\sim 47 \text{ mA cm}^{-2}$ for Co-bpy-BTC-750 with overpotential of 380mV versus $\sim 37 \text{ mA cm}^{-2}$ for Co-BTC-750 with overpotential of 455mV under identical conditions. The OER onset potential is lower for Co-bpy-BTC-750, indicating earlier reaction initiation and reduced kinetic barriers indicating the improved OER activity of the bipyridine-modified catalyst.

The performance gain is consistent with nitrogen incorporation during bipyridine modification. Introducing nitrogen increases electronic conductivity in the carbon matrix and perturbs the local cobalt coordination environment by introducing additional coordination sites and defect structures. These effects collectively facilitate charge transfer, increase the density of accessible active sites, and lower the effective overpotential for OER [27].

The lower onset potential and enhanced current density is attributed to reduced charge transfer resistance and optimized intermediates adsorption energies aligning with the recent reports on how nitrogen linker containing MOFs and bimetallic MOFs electronic structure improves OER kinetics implementing the crucial role of organic linker engineering in MOF based electrocatalysts. Recent studies have reported that nitrogen rich linkers like bipyridines can significantly lower the overpotential in Co-based MOFs in comparison to carboxylate only linkers. Khan et al. [28] studied the effect of pyridine like linkers on cobalt based metal organic frameworks and highlighted that these linkers stabilize the metal nodes in an MOF structure and increase accessible active site density resulting in improved conductivity via electron delocalization owing to defect site generation and electronic structure modulation. The synergy of enhanced conductivity and structural defects enabled by introducing bipyridine linker plays a key role in efficient water oxidation catalysis.

Besides the electronic effects, the morphological transformation like porosity, surface roughness,



electrolyte penetration and mass transport within the electrode framework induced by bipyridine accelerates the reaction kinetics. These effects collectively illustrate a promising strategy to overcome conductivity and stability limitations commonly observed in MOF electrocatalysis.

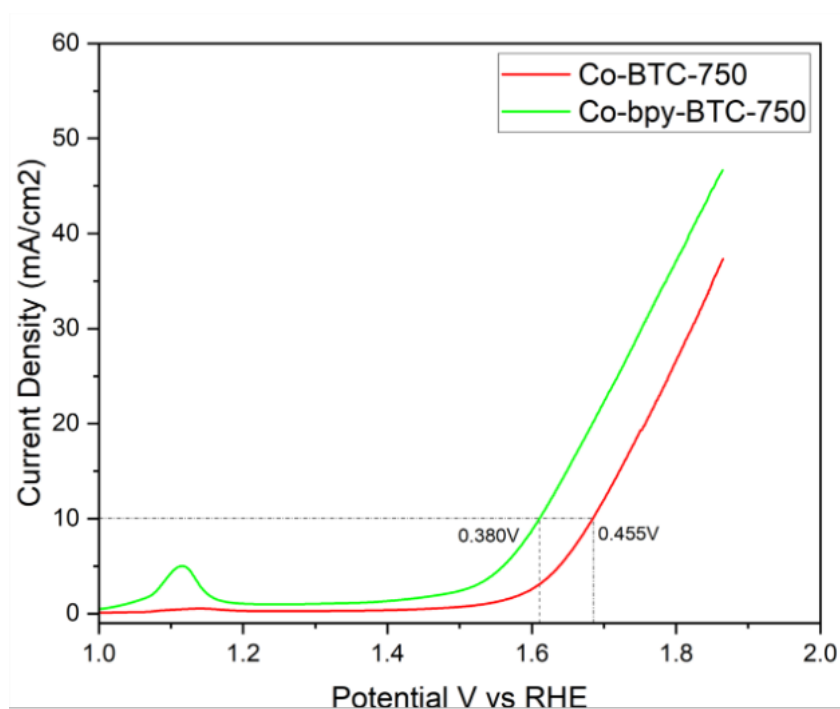


Figure 4 Electrochemical test via LSV confirming the superior electrochemical properties of Co-bpy-BTC-750 catalysts in comparison to Co-BTC-750

4. Conclusion

Cobalt-BTC and its bipyridine-modified analogue were synthesized and evaluated as MOF-derived precursors for oxygen-evolution electrocatalysts. Morphological and structural analyses show that introducing 2,2'-bipyridine perturbs the parent framework to yield a more defective, porous architecture while preserving long-range order, and thermal measurements indicate enhanced stability relative to Co-BTC. Electrochemical testing in alkaline media further demonstrates that the bipyridine-modified material delivers higher current densities at a lower onset potential than the BTC-only counterpart. The performance gain is consistent with nitrogen incorporation that improves charge transfer and increases the

density of accessible active sites. Taken together, these results establish ligand engineering with nitrogen-rich chelating ligands as a simple, scalable strategy for optimizing MOF-derived, binder-free OER catalysts for efficient water electrolysis.

References

1. Vidas, L. and R. Castro, *Recent developments on hydrogen production technologies: state-of-the-art review with a focus on green-electrolysis*. Applied Sciences, 2021. **11**(23): p. 11363.
2. Franco, A. and C. Giovannini, *Recent and future advances in water electrolysis for green hydrogen generation: Critical analysis and perspectives*. Sustainability, 2023. **15**(24): p. 16917.
3. Suen, N.-T., et al., *Electrocatalysis for the oxygen evolution reaction: recent development and future perspectives*. Chemical Society Reviews, 2017. **46**(2): p. 337-365.
4. Zhao, Y., et al., *Oxygen evolution/reduction reaction catalysts: from in situ monitoring and reaction mechanisms to rational design*. Chemical reviews, 2023. **123**(9): p. 6257-6358.
5. Sun, R., et al., *Recent advances in cobalt- talysts for efficient electrochemical hydrogen evolution: a review*. Dalton Transactions, 2022. **51**(40): p. 15205-15226.
6. Zhang, X., et al., *Rare-Earth Neodymium Doping Boosts the Catalytic Performance of Co3O4 for Acidic Water Oxidation*. Journal of Alloys and Compounds, 2025: p. 181103.
7. Dhakshinamoorthy, A., et al., *Cobalt-based metal organic frameworks as solids catalysts for oxidation reactions*. Catalysts, 2021. **11**(1): p. 95.
8. Rasheed, T., et al., *Metal-organic framework-based engineered materials—fundamentals and applications*. Molecules, 2020. **25**(7): p. 1598.
9. Shen, K., et al., *Development of MOF-derived carbon-based nanomaterials for efficient catalysis*. Acs Catalysis, 2016. **6**(9): p. 5887-5903.



10. Xiao, W., et al., *Functional metal/carbon composites derived from metal–organic frameworks: insight into structures, properties, performances, and mechanisms*. ACS Catalysis, 2023. **13**(3): p. 1759-1790.
11. Kharissova, O.V., et al., *Catalysis using metal–organic framework-derived nanocarbons: Recent trends*. Journal of Materials Research, 2020. **35**(16): p. 2190-2207.
12. Corma, A., H. Garcia, and F. Llabrés i Xamena, *Engineering metal organic frameworks for heterogeneous catalysis*. Chemical reviews, 2010. **110**(8): p. 4606-4655.
13. Liao, Y.-T., B.M. Matsagar, and K.C.-W. Wu, *Metal–organic framework (MOF)-derived effective solid catalysts for valorization of lignocellulosic biomass*. ACS Sustainable Chemistry & Engineering, 2018. **6**(11): p. 13628-13643.
14. Wiggins-Camacho, J.D. and K.J. Stevenson, *Effect of nitrogen concentration on capacitance, density of states, electronic conductivity, and morphology of N-doped carbon nanotube electrodes*. The Journal of Physical Chemistry C, 2009. **113**(44): p. 19082-19090.
15. Hou, Y., et al., *An advanced nitrogen -doped graphene/cobalt -embedded porous carbon polyhedron hybrid for efficient catalysis of oxygen reduction and water splitting*. Advanced Functional Materials, 2015. **25**(6): p. 872-882.
16. Xue, Z., et al., *Missing-linker metal-organic frameworks for oxygen evolution reaction*. Nature Communications, 2019. **10**(1): p. 5048.
17. Chen, T., et al., *Architecting Nanostructured Co-BTC@GO Composites for Supercapacitor Electrode Application*. Nanomaterials (Basel), 2022. **12**(18).
18. Diamond, B.A., Lillian%AHendon, Christopher%BJournal Name: Communications Chemistry, J.V. 6, and J.I. 1, *Ligand field tuning of d-orbital energies in metal-organic framework clusters*. Journal Name: Communications Chemistry; Journal Volume: 6; Journal Issue: 1, 2023: p. Medium: X.



19. Ambrose, B., et al., *Impact of Ligand in Bimetallic Co, Ni-Metal-Organic Framework towards Oxygen Evolution Reaction*. *Electrochimica Acta*, 2023. **439**: p. 141714.
20. Rajendran, N. and S. Karthikeyan, *Catalytic Applications of BTC-Based Metal–Organic Frameworks: Synthesis, Properties, and Mechanistic Insights*. *ACS Omega*, 2025.
21. Mauger-Sonnek, K., *Liquid sorption properties and structural changes of metal-organic frameworks of cobalt nitrate and 4, 4'-bipyridine*. 2013.
22. Ma, J., et al., *Defect engineering on metal-organic frameworks for enhanced photocatalytic reduction of Cr(VI)*. *Surfaces and Interfaces*, 2024. **54**: p. 105174.
23. Tian, F., et al., *Synthesis of bimetallic–organic framework Cu/Co-BTC and the improved performance of thiophene adsorption*. *RSC advances*, 2019. **9**(27): p. 15642-15647.
24. Chen, B., et al., *Thermal decomposition kinetics of M–BTC (M = Cu, Co, Zn, and Ce) and M–BTC/Pt composites under oxidative and reductive environments*. *Chemical Engineering Journal*, 2022. **450**: p. 138470.
25. Steenhaut, T., et al., *Synthesis, Structure, and Thermal Stability of a Mesoporous Titanium(III) Amine-Containing MOF*. *Inorg Chem*, 2022. **61**(29): p. 11084-11094.
26. Zhang, J., et al., *Research Progress of Cobalt-Based Metal Organic Frameworks and Their Derivatives in Energy Storage and Conversion*. *ACS Omega*, 2024. **9**(47): p. 46643-46663.
27. Hoefnagel, M.E. and D.G. Hettterscheid, *The Role of Metal–Organic Framework Induced Confinement Effects on Molecular Electrocatalysts Relevant to the Energy Transition*. *ChemSusChem*, 2025: p. 2402676.
28. Khan, J., A. Ahmed, and A.A. Al-Kahtani, *From design to efficiency: cobalt-based MOFs for efficient and stable electrocatalysis in hydrogen and oxygen evolution reactions*. *RSC advances*, 2025. **15**(11): p. 8420-8429.



Functionalized Halloysite Nanotube filled Poly (Vinyl Alcohol)/ Quaternized Chitosan as Bio-based Composite Polymer Membrane for Alkaline Electrolysis

*Phyo Min Zaw*¹, *Chutiwat Likitaporn*², *Peerawat Prathumrat*², *Thwelt Thinzar Zaw*¹, *Manunya Okhawilai*^{1,2*}

¹Nanoscience and Technology, Graduate School, Chulalongkorn University, Bangkok, 10330, Thailand

²Department of Chemical Engineering, Faculty of Engineering, Chulalongkorn University, Bangkok, 10330, Thailand

Corresponding Author E-mail: Manunya.O@chula.ac.th

ABSTRACT

The demand for sustainable materials in energy conversion motivates the development of high-performance, eco-friendly anion-exchange membranes (AEMs) for alkaline electrolysis. This study presents a new composite membrane based on poly(vinyl alcohol) (PVA) and quaternized chitosan (QCS), reinforced with functionalized halloysite nanotubes (HNTs), a superior alternative to conventional materials. The design integrates two strategies to enhance electrochemical properties. First, chitosan was chemically quaternized with glycidyltrimethylammonium chloride, introducing cationic sites and achieving a high degree of quaternization of 48% crucial for ion exchange. Second, HNTs were functionalized with γ -aminopropyltriethoxysilane (APTES) to increase surface amine groups, improving compatibility with the polymer matrix and facilitating hydroxide ion transport. The final membrane was fabricated by blending PVA and QCS at a 4:1 ratio with APTES-HNTs, forming a uniform, well-integrated matrix. Characterization confirmed successful modification and polymer–nanotube interactions, and electrochemical impedance spectroscopy demonstrated high ionic conductivity of 10 to 20 mS cm⁻¹. Alkaline uptake measurements further supported enhanced ion transport. The combined effects of quaternary ammonium groups in QCS and amine functionalities on HNTs create efficient pathways for hydroxide conduction. This PVA/QCS/APTES-HNT membrane presents a promising and durable material for alkaline electrolysis, representing a significant advancement in AEM design.

Keywords: Biopolymer Membrane, Quaternized Chitosan, Functionalized Halloysite Nanotubes, Alkaline Electrolysis.

Introduction

The global demand for clean energy in every life, from powering electric vehicles to providing electricity for homes and portable devices, has intensified interest in green hydrogen (H₂) as a sustainable energy carrier¹. Alkaline water electrolysis, a promising method for green H₂ production, requires high-performance anion exchange membranes (AEMs) that are efficient, durable, and environmentally friendly. Conventional AEMs typically rely on petroleum-based polymers and expensive fluorinated materials, motivating research into renewable, low-cost alternatives².

Bio-derived polymers such as chitosan and poly(vinyl alcohol) (PVA) have emerged as attractive candidates for AEM fabrication³. Chitosan, a deacetylated derivative of chitin, offers film-forming ability, biodegradability, and reactive amine groups that allow straightforward chemical modification⁴. Quaternization introduces permanent quaternary ammonium groups, significantly enhancing ionic conductivity by providing mobile OH⁻ hopping sites⁵. However, quaternized chitosan (QCS) alone is mechanically weak and prone to excessive swelling in aqueous environments, limiting its practical use⁵.

Composite approaches offer a solution. Blending QCS with PVA provides mechanical support, while hydroxyl groups of PVA and hydrogen-bonding network improve film stability and water tolerance^{6,7}. To further enhance robustness and ion transport, we incorporate halloysite nanotubes (HNTs), naturally occurring aluminosilicate nanotubes, functionalized with γ -aminopropyltriethoxysilane (APTES). The amino-functionalized HNTs (APTES-HNTs) improve compatibility with the polymer matrix and participate in ion transport pathways. One-dimensional nanofillers such as these materials are known to enhance mechanical strength and create additional ion pathways, especially when functionalized with hydrophilic or cationic groups⁶. For example, Shi *et al.*⁶ demonstrated that quaternized HNTs embedded in chitosan increased hydroxide conductivity by 89% compared to the polymer alone.

Based on these insights, this research employs a hierarchical approach to address the dual challenges of ionic conductivity and mechanical robustness. First, CS is quaternized to introduce fixed cationic groups,



promoting OH⁻ transport⁸. Second, the PVA matrix is reinforced with APTES-HNTs to limit swelling and enhance ion transport. This multipronged design combines chemical modification, polymer blending, and nanofiller incorporation to create an AEM with improved performance and stability, offering practical pathway for green H₂ production in everyday energy applications⁹.

Materials and methods

1. Materials

Chitosan (from shrimp shell, degree of deacetylation $\approx 95\%$) was obtained from Marine Bio Resources Co. (Thailand). Glycidyl trimethylammonium chloride (GTMAC, laboratory grade $\sim 90\%$ purity), halloysite nanotubes (HNT) powder, γ -aminopropyltriethoxysilane (APTES, $\geq 99\%$), and glutaraldehyde (GA, 25% solution in water) were purchased from Sigma-Aldrich (USA). Sulfuric acid (H₂SO₄) (concentrated 95–98%, ACS grade), toluene (anhydrous, $\geq 99.8\%$), were purchased from Loba Chemie Pvt. Ltd (India). Glacial acetic acid ($\geq 99\%$, analytical grade) was purchased from Sigma-Aldrich (Germany). Silver nitrate (AgNO₃) was purchased from Fisher Chemical (UK). Potassium chromate (K₂CrO₄) indicator was purchased from Tokyo Chemical Industry Co., Ltd (Japan). Acetone was purchased from Biotech and Scientific Co Ltd (Thailand), and ethyl alcohol was purchased from Chemex (Thailand).

2. Synthesis and functionalization

2.1 Quaternization of chitosan (QCS)

As depicted in **Figure 1(a)**, QCS was synthesized by reacting to the primary amine groups of chitosan with GTMAC. Briefly, CS was first dissolved in a 2% (v/v) aqueous acetic acid solution to form a homogeneous solution, after which GTMAC was added at a predetermined molar ratio. The reaction was conducted under vigorous stirring at 70 °C for 24 hours. The resulting QCS solution was then precipitated in excess cold



acetone, thoroughly washed with ethanol to remove unreacted species and byproducts, and dried in an oven at 50 °C to yield QCS powder. The degree of quaternization (DQ) was controlled by adjusting the initial GTMAC-to-glucosamine molar ratio.

2.2 Functionalization of halloysite nanotubes (APTES-HNT)

The surface of HNTs was functionalized with APTES as illustrated in **Figure 1(b)**. Initially, HNTs were acid-etched in 1 M H₂SO₄ at 70 °C for 12 hours, followed by vacuum filtration and repeated washing with deionized (DI) water until the pH reached neutral. The treated HNTs were then dried in a vacuum oven at 80 °C for 24 hours. Subsequently, the resulting HNTs were dispersed in toluene using ultrasonication, after which APTES were introduced, and the suspension was refluxed at 120 °C for 24 hours. During this process, the silane groups of APTES hydrolyzed and condensed with surface hydroxyl groups of the HNTs, forming covalent Si-O-Si and Si-O-Al linkages¹⁰. Finally, the functionalized APTES-HNTs were collected by centrifugation, thoroughly washed with toluene and ethanol to remove excess unreacted silane, and dried again in a vacuum oven at 80 °C overnight¹¹.

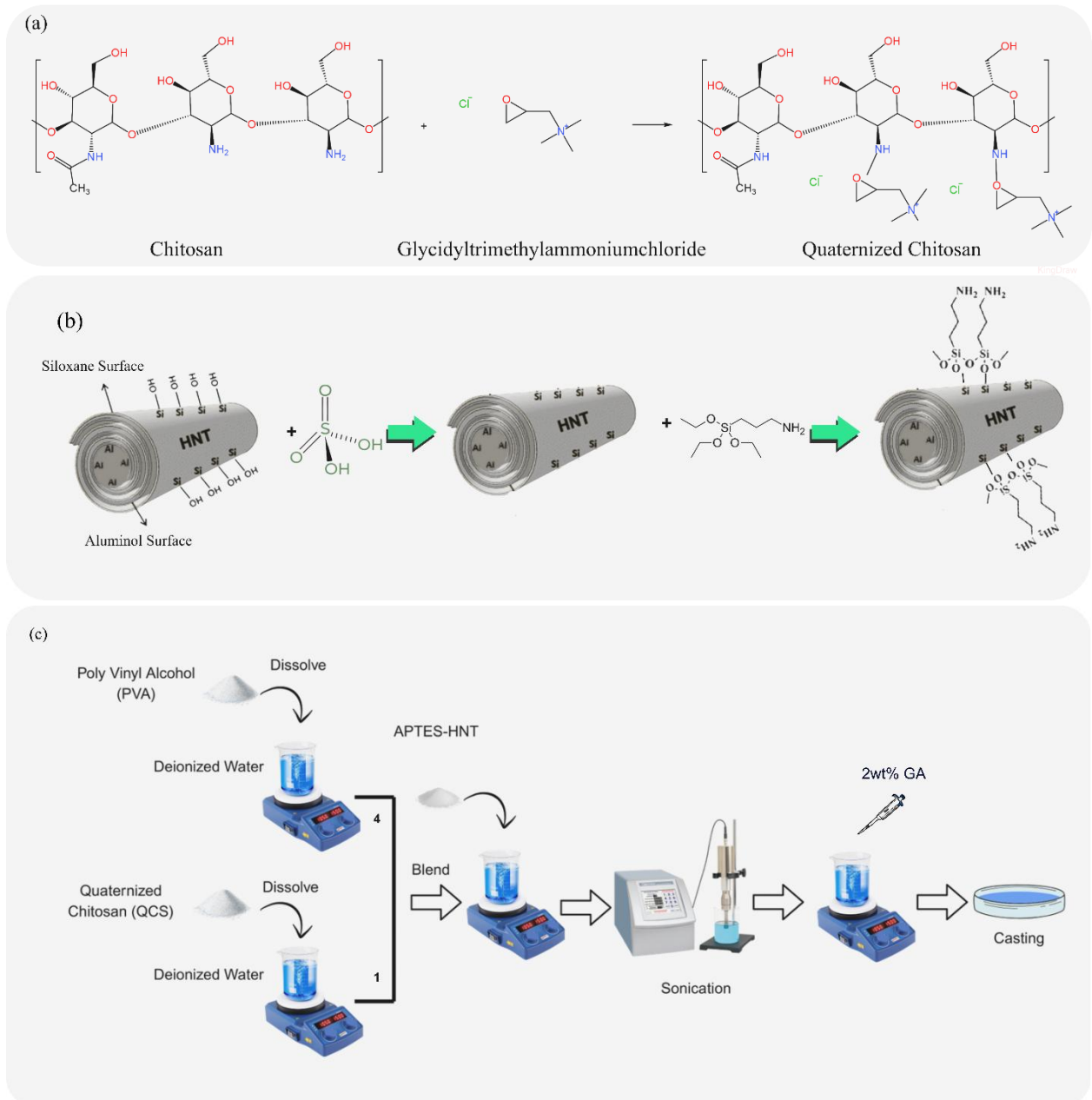


Figure 1: Methods of: (a) Quaternization of chitosan, (b) Functionalization of HNT, and (c) Solution casting.

3. Membrane fabrication

The biocomposite polymer membranes were prepared using a solution casting method, schematically shown in **Figure 1(c)**. First, PVA was dissolved in DI water at 90 °C to obtain a clear solution, while QCS was



separately dissolved at 70 °C. The two polymer solutions were then mixed at a mass ratio of 4:1 and stirred until a homogeneous PVA/QCS blend was achieved. A specified amount of APTES-HNT powder was dispersed into the blend using ultrasonication to ensure uniform distribution, followed by the addition of 2wt% GA solution for 30 minutes prior to casting. The resulting viscous mixture was cast onto a Teflon mold and dried at 50 °C for 24 hours to allow slow solvent evaporation. The membrane was carefully peeled from the mold and stored in a sealed bag for further testing and characterization. For comparison, a control PVA/QCS membrane without APTES-HNT was prepared using the same procedure.

4. Characterization

4.1. Degree of quaternization (DQ)

The DQ, defined as the fraction of chitosan amino groups converted into quaternary ammonium salt, was determined by a chloride ion titration method. Since the quaternary ammonium substituents in QCS exist as chloride salts ($-N^+(CH_3)_3Cl^-$), each quaternized unit contributes to one Cl^- counterion¹². To quantify this, 100 mg of QCS was dissolved in 50 mL of distilled water and titrated with 0.1 M $AgNO_3$ using **Mohr's method**. A few drops of 0.25 M K_2CrO_4 solution were added as an indicator. The titration was continued until a permanent reddish-brown color appeared, signifying the precipitation of all Cl^- as $AgCl$ and the formation of Ag_2CrO_4 at the first excess of Ag^+ ¹³. The volume of $AgNO_3$ consumed was then used to calculate the moles of Cl^- , which directly corresponded to the moles of quaternary ammonium groups.

DQ calculation formula¹²:

$$DQ(\%) = \frac{\frac{CV}{1000}}{\frac{CV}{1000} + \frac{W \cdot \left(\frac{CVM_2}{1000}\right)}{M_1}} \times 100 \quad (1)$$

Where C is the concentration of $AgNO_3$ is expressed in $mol \cdot L^{-1}$, V is the volume of $AgNO_3$ used is measured in milliliters (mL), and W is the mass of QCS sample used in the titration is given in grams (g). M_1 is the molar mass of the glucosamine unit, and is $161.2 \text{ g} \cdot \text{mol}^{-1}$, while M_2 the molar mass of the quaternized unit which is $312.8 \text{ g} \cdot \text{mol}^{-1}$.

4.2. Spectroscopic and microscopic analysis: Fourier-Transform Infrared (FTIR) Spectroscopy (ParkinElmer, SpectrumGX, Japan) with a wavenumber range of 4000-400 cm^{-1} was used to identify chemical structures and functional groups with KBr (Potassium Bromide) disc/pellet method for powders. Nicolet™ iS™ 10 FTIR Spectrometer (ThermoFisher Scientific) is used to identify chemical structures and functional groups with Attenuated Total Reflectance (ATR-mode) for the membrane. The surface morphology of the membranes was examined using field scanning electron microscopy (FESEM, Quanta 250 FEG), while their elemental compositions were analyzed with an energy dispersive X-ray spectroscopy (EDS).

4.3. Electrochemical evaluation

Ionic conductivity: Hydroxide conductivity was measured using AC impedance spectroscopy (PalmSens4, The Netherlands). Before testing, the membranes were converted to the OH^- form by immersion in 1 M KOH for 48 hours, followed by thorough rinsing with DI water. The hydrated membranes were placed in a two-electrode conductivity cell under 100% relative humidity. Impedance spectra were recorded over a frequency range of 1 Hz to 1 MHz. The membrane resistance (R , Ω) was determined from the high-frequency intercept of the Nyquist plot with the real axis. The ionic conductivity (σ , S cm^{-1}) was calculated using the following equation:

$$\sigma = \frac{L}{(R \times A)} \quad (2)$$

where L is the membrane thickness (cm) and A is the electrode area (cm^2).

Swelling ratio and alkali uptake: Dry membrane samples (W_{dry}) were first weighed and then immersed at room temperature for 24 hours in either DI water (for swelling ratio) or 1 M KOH solution (for alkaline uptake). After equilibration, the samples were removed, gently blotted to remove surface moisture, and immediately reweighed to obtain wet weight (W_{wet}) or alkaline-soaked weight (W_{alkaline}).

$$\text{Swelling ratio (\%)} = \frac{W_{\text{wet}} - W_{\text{dry}}}{W_{\text{dry}}} \times 100 \quad (3)$$

$$\text{Alkaline uptake (\%)} = \frac{W_{\text{alkaline}} - W_{\text{dry}}}{W_{\text{dry}}} \times 100 \quad (4)$$

Results and discussion

The successful synthesis of the composite AEM and its enhanced properties were verified through a systematic analysis of its chemical structure, morphology, and electrochemical performance.

1. Chemical structure verification via FTIR spectroscopy

FTIR spectroscopy provided clear evidence of the chemical transformations leading to the composite membrane, as presented in **Figure 2(a)**. For QCS, a strong absorption band at 1480 cm^{-1} , absent in neat CS, was attributed to the C–H bending vibrations of newly introduced trimethylammonium groups⁴. This peak served as a definitive signature of successful quaternization, confirming the grafting of GTMAC onto the CS backbone. Additionally, the broad O–H/N–H stretch band at $3500\text{--}3200\text{ cm}^{-1}$ becomes slightly weaker or shifted, indicating altered hydrogen-bonding interactions upon quaternization. These results confirmed that CS was successfully quaternized into QCS, suitable for use as an ion-conducting polymer.

Evidence of silane functionalization was obtained from the FTIR spectra of unmodified and APTES-HNTs, as shown in **Figure 2(b)**. The neat HNT showed characteristic Si–O (bending, 1034 cm^{-1}), Al–OH (bending, 940 cm^{-1})¹⁴. New peaks appeared after APTES treatment, including C–H stretching vibrations at $2930\text{--}2900\text{ cm}^{-1}$, C–H bending at $1500\text{--}1460\text{ cm}^{-1}$, and N–H bending at $1575\text{--}1565\text{ cm}^{-1}$. These features corresponded to the propyl chains and primary amine groups of the grafted APTES, confirming the successful formation of $\text{NH}_2\text{-HNT}$ ¹⁵.

The final crosslinked PVA/QCS/HNT membrane spectrum, as depicted in **Figure 2(c)**, reflected contributions for all components and crosslinking reactions. The quaternary ammonium C–H bend at 1480 cm^{-1} from QCS showed that QCS was retained within the membrane⁴. Reduced C–H and N–H bands from the $\text{NH}_2\text{-HNT}$ at 2930 and 1570 cm^{-1} indicated that the nanotubes were embedded in the polymer matrix¹⁵. New band at 1640 cm^{-1} assigned to C=N stretching, is the evidence of imine linkages⁴. The C=O stretching peaks observed in the $1500\text{--}1700\text{ cm}^{-1}$ region of the FTIR spectra indicate the presence of carbonyl



functional groups, which are primarily attributed to the formation of new chemical bonds during membrane synthesis. The simultaneous presence of imine linkages and quaternary ammonium groups confirmed that crosslinking occurred without reducing the integrity of QA groups⁴.

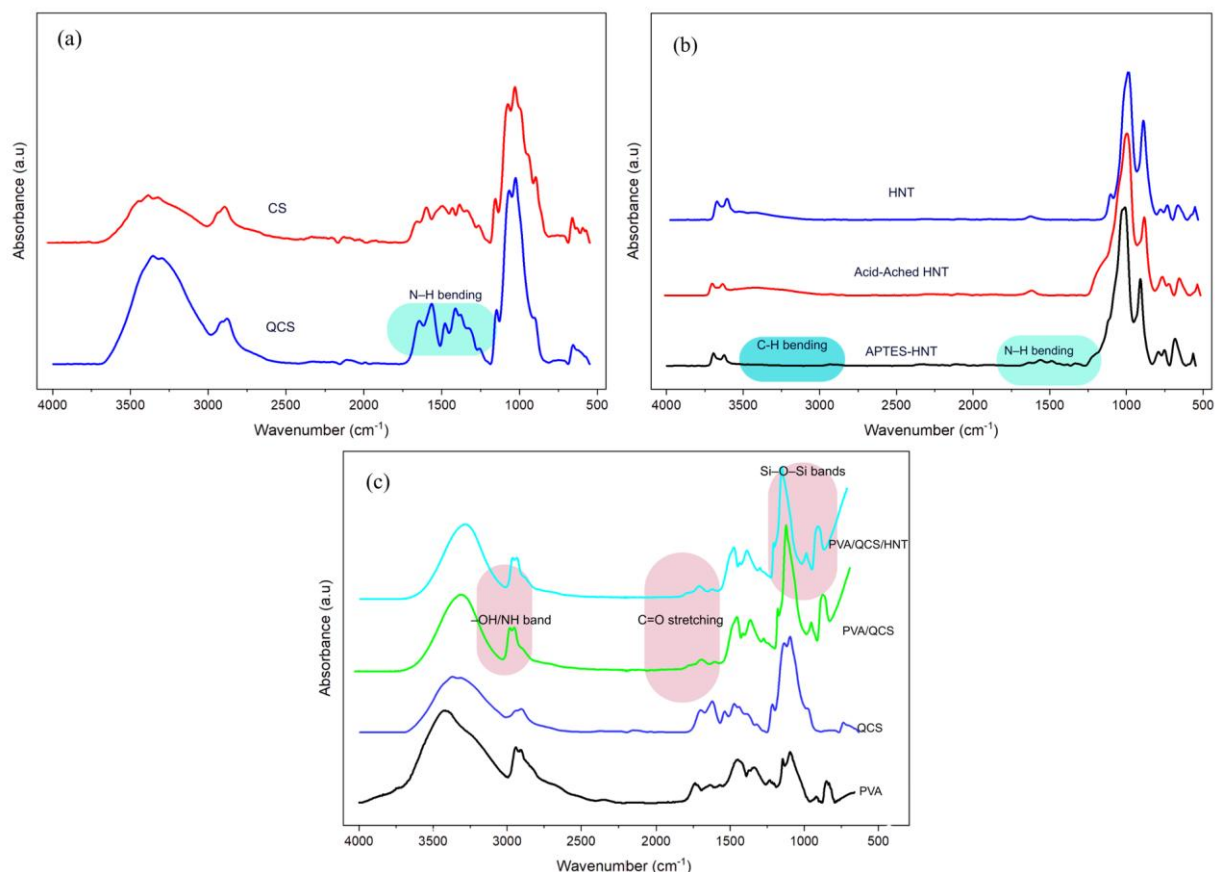


Figure 2. FTIR Spectra of (a) neat CS and QCS, (b) HNTs and APTES-HNTs, (c) PVA/QCS/APTES-HNT composite membrane compared with its various components.

2. Morphological and compositional characterization

The morphology of HNTs and functionalized APTES-HNTs are investigated by SEM and EDS, as shown in **Figure 3(a), (b)**. HNTs are naturally occurring aluminosilicate clays, composed of Al and Si. The uniform presence of these elements across the EDS mapping confirmed the successful incorporation of HNTs into the membrane. More significantly, evidence for the APTES functionalization was provided by the co-localization of N and Si signals as in **Figure 3(c)**. While Si originated from both the HNT structure and



silane groups of APTES, the detection of N, unique to the terminal amine group in APTES, overlapping with Si strongly indicated that APTES molecules were successfully grafted onto the HNTs as shown in **Figure 3(d)** and its respective EDS mappings.

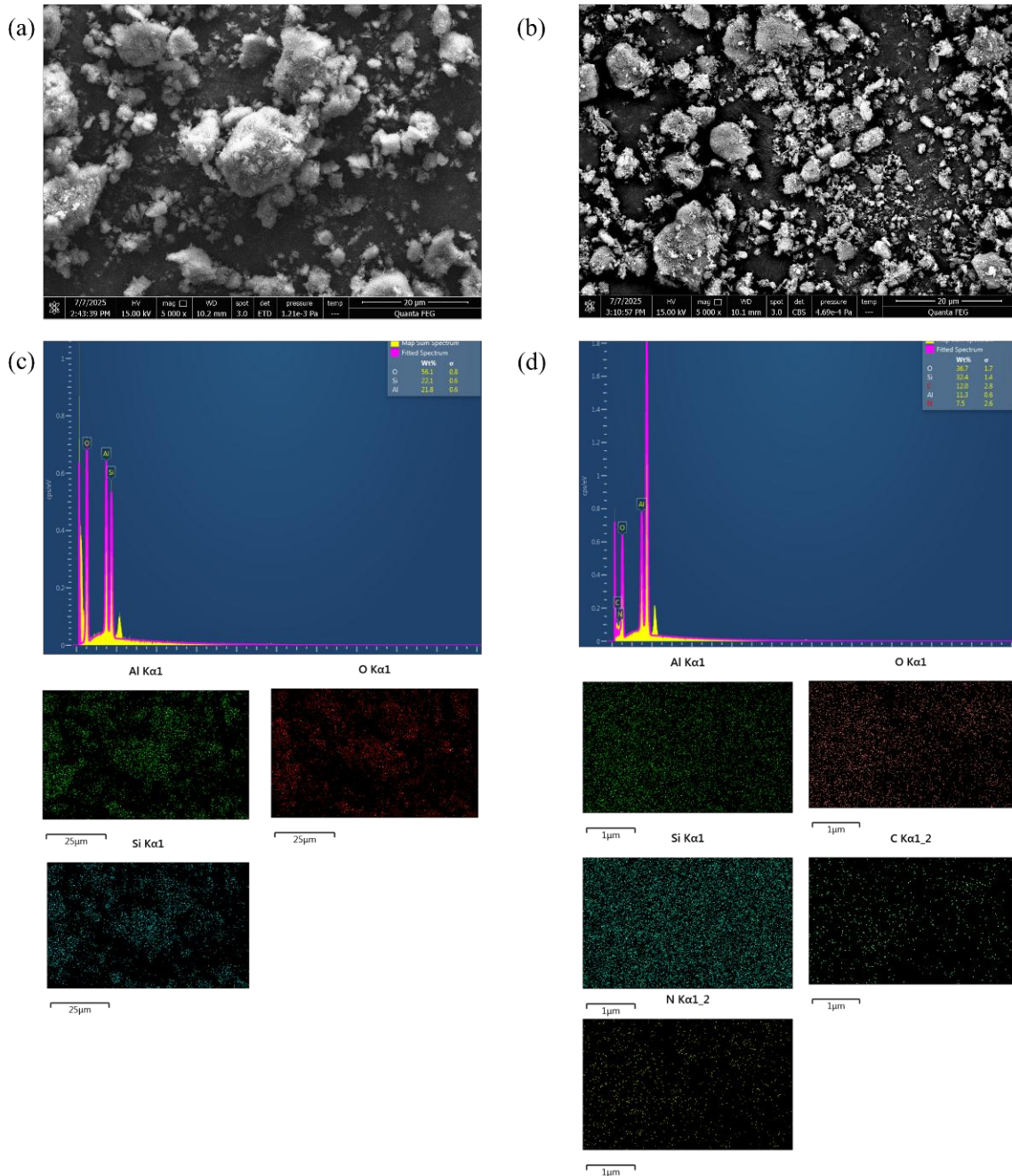


Figure 3. FESEM image and EDS elemental mappings (a) FESEM image of HNT (b) FESEM image of APTES-HNT (c) EDS and mapping of HNT (d) EDS and mapping of APTES-HNT

Degree of quaternization (DQ)

DQ was calculated by using **Equation (1)**. The titrated amount of AgNO_3 was recorded in ml and calculated values of DQ are mentioned in the table below. These values are satisfactory to have enough cationic conductivity within the membrane ¹⁶.

Table 1: Degree of quaternization of chitosan

Samples	Amount of AgNO_3 (ml)	DQ (%)
QCS_1	2.0	46.28
QCS_2	2.1	49.65

3. Electrochemical and physicochemical performance

3.1 Ionic conductivity

The incorporation of HNT into the PVA/QCS matrix enhanced ionic transport, as indicated in **Figure 4(a)**. The ionic conductivity of the PVA/QCS/HNT composite, calculated by **Equation (2)**, reached $0.015 \pm 0.004 \text{ S cm}^{-1}$, compared with only $0.006 \pm 0.002 \text{ S cm}^{-1}$ for the neat PVA/QCS membrane, representing an increase of about two- to threefold. This enhancement likely arose from well-dispersed nanochannels of HNTs, which reduced polymer crystallinity and promoted water retention, facilitating ion mobility. Such behavior aligned with prior reports on halloysite-based fillers and highlighted the potential of the PVA/QCS/HNT membrane as a more efficient anion-exchange or fuel-cell electrolyte.



3.2. Dimensional stability in alkaline environments

Swelling ratio

The addition of APTES-HNT slightly enhanced the swelling behavior of the membranes. The PVA/QCS membrane exhibited a swelling ratio of 140%, while the PVA/QCS/HNT composite reached approximately 150%, calculating using **Equation (3)**. These results corresponded to a 10% increase in equilibrium swelling, as presented in **Figure 4(b)**. This modest increase suggested a slightly higher water uptake or free volume in the composite. Significantly, the relatively small change indicated that the HNT-filled composite membrane maintained good structural stability while benefiting from marginally increased hydration.

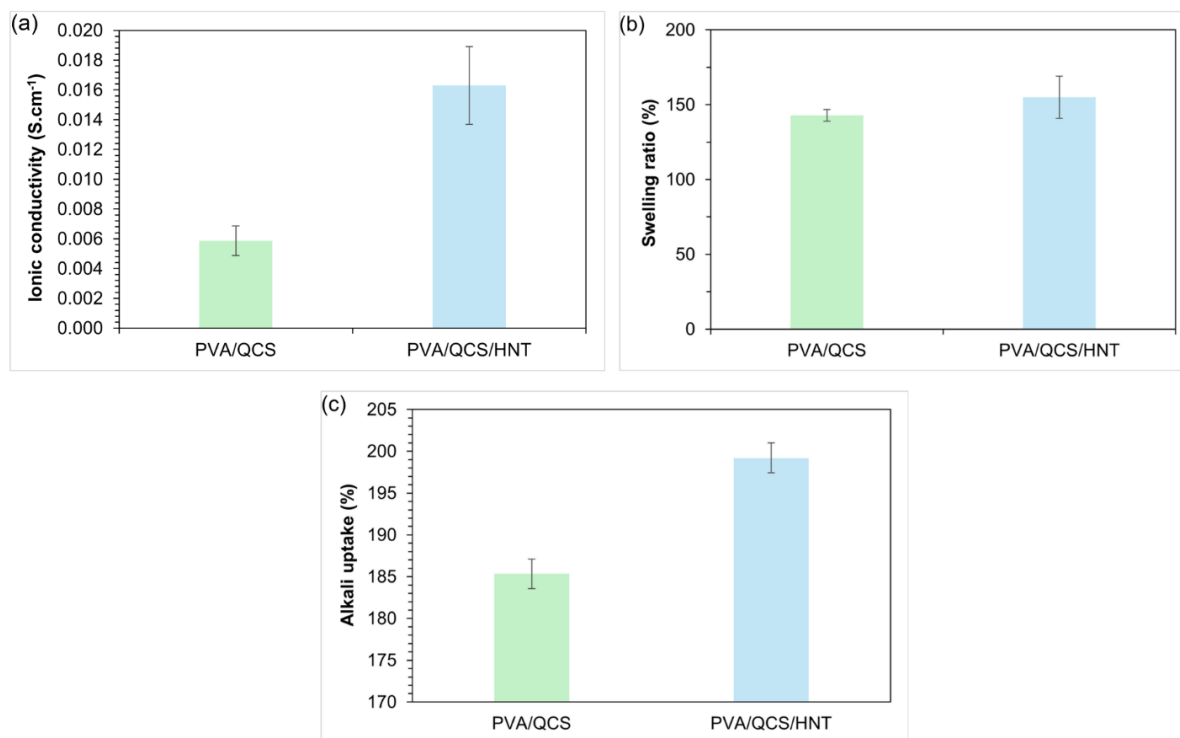


Figure 4 Electrochemical data (a) ionic conductivity, (b) swelling ratio, and (c) alkali uptake

Alkali uptake

Alkaline uptake is further enhanced by HNT incorporation, as calculated using **Equation (4)**. **Figure 4(c)** indicates that the PVA/QCS membrane absorbed about 185%, whereas the PVA/QCS/HNT composite



reached 200%, which was an increase of 15%. The higher uptake implied that the HNT-containing membrane could accommodate more OH^- under the same conditions, likely due to the aluminosilicate tubes providing additional adsorption sites or altering the polymer network⁴. In practice, improved alkaline uptake typically corresponded to higher ion-exchange capacity and enhanced alkaline stability, indicating that the PVA/QCS/HNT composites could maintain higher ionic conductivity under alkaline conditions.

Conclusion

This study demonstrates the synthesis of a new AEM comprising a PVA/QS matrix reinforced with APTES-HNTs. By transforming HNTs from passive fillers into multifunctional components, the composite achieves robust mechanical reinforcement while enabling synergistic ion transport pathways. The PVA/QCS/APTES-HNT membrane exhibited significantly enhanced ionic conductivity alongside controlled swelling ratio and alkaline uptake compared to the neat PVA/QCS membrane. These results highlighted that the combination of a sustainable bio-based matrix, chemical functionalization, and nanoscale reinforcement was a powerful approach for overcoming the conductivity-stability trade-off in AEMs. The material showed strong potential for a low-cost, durable alkaline electrolyzer, with future work focusing on optimizing nanofiller loading, membrane-electrode assembly fabrication, and long-term performance evaluation.

Author Contributions

The manuscript was written through contributions of all authors. All authors have given approval to the final version of the manuscript.

Acknowledgments

The authors gratefully acknowledge the financial support from The Program Management Unit for Human Resources & Institutional Development, Research and Innovation (B49G680115), The second Century



Fund (C2F), Chulalongkorn University, and National Research Council of Thailand (NRCT) and Chulalongkorn University (N42A680292).

5. References

- 1 Cho, MK, Lim, A, Lee, SY, Kim, H-J, Yoo, SJ, Sung, Y-E, Park, HS & Jang, JH. A Review on Membranes and Catalysts for Anion Exchange Membrane Water Electrolysis Single Cells. *J. Electrochem. Sci. Technol* **8**, 183-196 (2017).
- 2 Karibayev, M, Myrzakhmetov, B, Kalybekkyzy, S, Wang, Y & Mentbayeva, A. Binding and Degradation Reaction of Hydroxide Ions with Several Quaternary Ammonium Head Groups of Anion Exchange Membranes Investigated by the DFT Method. *Molecules* **27**, 2686 (2022).
- 3 Zhou, Y, Huang, Z, Deng, B, Gong, C & Liu, H. Biomass composite anion exchange membranes based on quaternized chitosan incorporated with imidazole ionic liquid-functionalized cellulose nanocrystals. *Polym. Eng. Sci.* **65**, 647-658 (2025).
- 4 Akhmetova, A, Myrzakhmetov, B, Wang, Y, Bakenov, Z & Mentbayeva, A. Development of Quaternized Chitosan Integrated with Nanofibrous Polyacrylonitrile Mat as an Anion-Exchange Membrane. *ACS Omega* **7**, 45371-45380 (2022).
- 5 Liu, G, Tsen, W-C, Jang, S-C, Hu, F, Zhong, F, Zhang, B, Wang, J, Liu, H, Wang, G, Wen, S & Gong, C. Composite membranes from quaternized chitosan reinforced with surface-functionalized PVDF electrospun nanofibers for alkaline direct methanol fuel cells. *J. Membr. Sci.* **611**, 118242 (2020).
- 6 Shi, B, Li, Y, Zhang, H, Wu, W, Ding, R, Dang, J & Wang, J. Tuning the performance of anion exchange membranes by embedding multifunctional nanotubes into a polymer matrix. *J. Membr. Sci.* **498**, 242-253 (2016).
- 7 Muhamad Samsudin, A, Bodner, M & Hacker, V. A Brief Review of Poly(Vinyl Alcohol)-Based Anion Exchange Membranes for Alkaline Fuel Cells. *Polymers* **14**, 3565 (2022).



- 8 Ryu, J, Seo, JY, Choi, BN, Kim, W-J & Chung, C-H. Quaternized chitosan-based anion exchange membrane for alkaline direct methanol fuel cells. *J. Ind. Eng. Chem.* **73**, 254-259 (2019).
- 9 Bao, Z, Yan, Y & Han, W. Investigation of γ -Aminopropyltriethoxysilane (APTES)-Modified Halloysite Nanotubes on the Reinforcement of Halloysite/Polypropylene (PP) Nanocomposites. *Polymers* **16** (2024).
- 10 Park, S, Yang, E, Park, H & Choi, H. Fabrication of functionalized halloysite nanotube blended ultrafiltration membranes for high flux and fouling resistance. *Environ. Eng. Res.* **25**, 771-778 (2020).
- 11 Verma, D, Okhawilai, M, Senthilkumar, N, Subramani, K, Incharoensakdi, A, Raja, GG & Uyama, H. Augmentin loaded functionalized halloysite nanotubes: A sustainable emerging nanocarriers for biomedical applications. *Environ. Res.* **242**, 117811 (2024).
- 12 Eren Belgin, E & Delibalta, CG. Quaternized chitosan/PVA/natural bioactive agent electrospun wound scaffolds: production, characterization, and investigation of release kinetics. *Turk J Chem* **47**, 1529-1539 (2023).
- 13 Wu, J-Y, Wang, C-Y, Chen, K-H, Lai, Y-R, Chiu, C-Y, Lee, H-C & Chang, Y-K. Electrospinning of Quaternized Chitosan-Poly(vinyl alcohol) Composite Nanofiber Membrane: Processing Optimization and Antibacterial Efficacy. *Membranes* **12** (2022).
- 14 Bekin Acar, S, Ozdemir, K, Mustapha, R & Mohammed, L. Thermoset nanocomposites reinforced by vinyl-functionalized halloysite. *Polym. Compos.* **44**, 148-155 (2022).
- 15 Song, L, Tan, K, Ye, Y, Zhu, B, Zhang, S & Huang, W. Amine-Functionalized Natural Halloysite Nanotubes Supported Metallic (Pd, Au, Ag) Nanoparticles and Their Catalytic Performance for Dehydrogenation of Formic Acid. *Nanomaterials* **12** (2022).
- 16 Myrzakhmetov, B, Akhmetova, A, Bissenbay, A, Karibayev, M, Pan, X, Wang, Y, Bakenov, Z & Mentbayeva, A. Review: chitosan-based biopolymers for anion-exchange membrane fuel cell application. *R. Soc. Open Sci.* **10**, 230843 (2023).



Improving Coulombic Efficiency in Anthraquinone–Bromine Flow Batteries with an Aqueous Bromine Complexant

P. Areebumrungsuk¹, P. Tangthum², M. Suttipong³, S. Kheawhoom^{1,}*

¹Department of Chemical Engineering, Faculty of Engineering, Chulalongkorn University, Bangkok 10330, Thailand

²Department of Chemical Technology, Faculty of Science, Chulalongkorn University, Bangkok 10330, Thailand

*Corresponding Author E-mail: Soorathep.K@chula.ac.th

ABSTRACT

Anthraquinone–bromine redox flow batteries (AQBFs) promise aqueous, low-cost energy storage but suffer bromine volatility, crossover, and parasitic reactions that lower coulombic efficiency and complicate operation. We evaluate 3-chloro-2-hydroxypropyltrimethylammonium chloride (CHA), a water-soluble quaternary ammonium, as a bromine-complexing additive that eliminates the need for persistent oil-phase management. Flow-cell tests (16 cm²) compared cells with and without CHA at 40–80 mA cm⁻² under identical electrolytes, membranes, and cycling protocols. With CHA, coulombic efficiency reached 90.68%, 88.51%, and 87.18% at 40, 60, and 80 mA cm⁻², respectively, exceeding the additive-free control at each current density. At 40 mA cm⁻², voltage and energy efficiencies were 49.98% and 45.32% with CHA versus 45.49% and 33.47% without additive. At 60–80 mA cm⁻², CHA yielded lower voltage and energy efficiencies than the control, indicating a current-dependent trade-off associated with increased polarization. Qualitatively, CHA reduced catholyte loss and intermittent oil-phase formation relative to the control. These results establish CHA as a practical, fully aqueous complexant that enhances coulombic efficiency and simplifies routine operation in AQBFs, while clarifying conditions under which voltage and energy efficiency penalties emerge. The findings provide a balanced basis for selecting bromine-management strategies in anthraquinone–bromine systems. All conclusions are supported exclusively by data already present in this original study.

Keywords: Anthraquinone-bromine flow battery; Bromine complexing agent; Energy storage;

Introduction

Energy storage technologies are central to the large-scale integration of renewable power and the attendant reduction of CO₂ emissions [1]. Among available options, aqueous redox flow batteries (RFBs) are particularly attractive for grid applications because they are intrinsically scalable, exhibit high safety, decouple power from energy capacity, and can deliver long cycle life with competitive efficiencies [2,3]. Within this class, AQBFB, an all-liquid, metal-free, organic–inorganic system, employs anthraquinone as the anolyte redox-active species and leverages earth-abundant constituents, fast redox kinetics, and pH-tunable chemistry [3-5]. Operation near neutral pH further suppresses parasitic pathways associated with strongly acidic or alkaline media [6,7]. Despite the favorable attributes of a bromine catholyte (high redox potential, high solubility, low cost), practical deployment is constrained by bromine volatilization, corrosiveness, and cross-diffusion, which elevate safety risks, accelerate self-discharge and active-material loss, shorten cycle life, and depress coulombic efficiency (CE).

A prevalent mitigation strategy employs quaternary ammonium salts—most notably N-methyl-N-ethylpyrrolidinium bromide (MEPBr)—to complex bromide/polybromide species into an immiscible oil phase and thereby lower bromine vapor pressure [8-10]. However, phase separation can hinder mass transport, complicate state-of-charge control, and increase maintenance burdens for pumps and piping. These limitations indicate a clear research need for low-cost, fully aqueous complexants that suppress bromine volatility and active-species escape without generating an oil phase, while preserving performance under neutral-pH AQBFB conditions.

Motivated by this gap, we posit that CHA, a commercially available, water-soluble quaternary ammonium, can electrostatically associate with bromide and polybromide species while remaining completely miscible in the aqueous phase; the hydroxyl functionality is expected to enhance solubility, reduce phase separation, and thereby suppress bromine vapor pressure and species loss [11]. In contrast to oil-phase complexants, this approach targets bromine management without creating a separate organic phase.



To test this premise, we evaluate an AQBFB using anthraquinone-2,7-disulfonic acid disodium salt (AQDS) as anolyte and Br₂-derived species as catholyte, and assess CHA as a bromine-complexing additive under otherwise identical conditions. The work advances the field by articulating an aqueous-complexant design rationale for neutral-pH AQBFBs, by providing a cell-level comparison of CHA against an additive-free control across practical current densities, and by quantifying CE, voltage efficiency (VE), and energy efficiency (EE) to clarify current-dependent trade-offs; in addition, qualitative observations indicate minor oil-phase formation and improved day-to-day operability. Collectively, these results suggest that CHA can enhance CE while minimizing operational burdens linked to phase separation, thereby improving the reliability and maintainability of AQBFBs for grid-scale storage.

Experimental Methods

AQBFB single-cell hardware consisted of two carbon-felt electrodes (4 cm × 4 cm; geometric area 16 cm²) separated by a cation-exchange membrane (Nafion-117) and connected to by copper current collectors (Figure 1). For each experiment, 100 mL of anolyte and 100 mL of catholyte were prepared. The anolyte contained 0.125 M anthraquinone-2,7-disulfonic acid disodium salt (AQDS) and 0.25 M NH₄OAc, adjusted to neutral pH. The catholyte contained 0.5 M NaBr and 1 M NH₄Br; 0.25 M CHA was added as a bromine-complexing agent. During operation, the electrolytes were continuously pumped through the flow cell.

The battery performance of AQBFB was evaluated through charge and discharge cycles for 5 cycles at current densities of 40, 60, and 80 mA cm⁻², with cutoff voltages at 2 V for charging and 0.2 V for discharging.

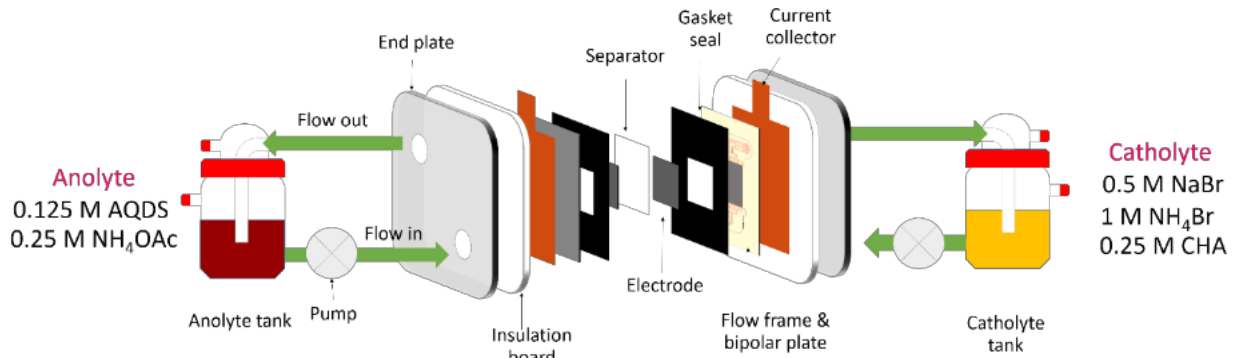


Figure 1. Single-cell schematic of AQFBF showing carbon-felt electrodes (4×4 cm; 16 cm^2), a Nafion-117 cation-exchange membrane, and external recirculating electrolyte loops.

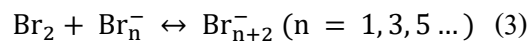
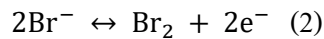
Theoretical Basis

During charging of AQFBF, the redox processes are described by Equations (1)–(4):

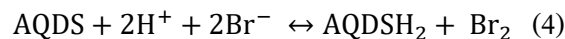
Anode side:



Cathode side:



Overall reaction:



During the charging step, AQDS is reduced to AQDSH₂ at the anode (Equation 1), while bromide is oxidized to molecular bromine at the cathode (Equation 2). The generated Br₂ undergoes rapid, reversible complexation to form polybromide anions (Equation 3; e.g., Br₃⁻, Br₅⁻), which are consumed in the reverse direction during discharge. Because molecular bromine possesses a high vapor pressure, accumulation of free Br₂ can result in volatilization and loss of active-material. Consequently, bromine-complexing agents are employed to shift speciation toward bound polybromides, thereby suppressing the effective activity of Br₂ [8].

In this study, we introduce CHA as a low-cost, commercially available bromine-complexing agent (Figure 2). The quaternary ammonium cation in CHA promotes strong electrostatic interactions with bromide and polybromide species, while the hydroxyl moiety enhances aqueous solubility and discourages phase separation. Together, these features favor the formation of CHA-Br_n ion pairs in the aqueous phase, lowering the free Br₂ concentration and its tendency to partition into the headspace, thereby mitigating the loss of active-species [11].

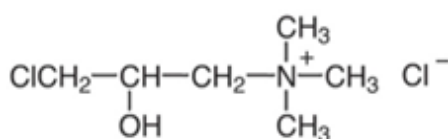


Figure 2. Molecular structure of CHA.

Theoretical Calculations

The coulombic efficiency (CE), which is the efficiency with which a battery stores and releases charge, can be calculated using Equation (5):

$$\text{Coulombic efficiency (CE)} = \frac{\text{Discharge capacity}}{\text{Charge capacity}} \times 100\% \quad (5)$$

The voltage efficiency (VE), which represents the efficiency of voltage usage during the charge and discharge cycles, can be calculated using Equation (6):

$$\text{Voltage efficiency (VE)} = \frac{\text{Average discharge voltage}}{\text{Average charge voltage}} \times 100\% \quad (6)$$

The energy efficiency (EE), which is the overall efficiency of energy recovery during cycle, can be calculated using Equation (7):

$$\text{Energy efficiency (EE)} = \text{CE} \times \text{VE} \quad (7)$$

Results

Two AQBFBs, without and with the CHA additive, were galvanostatically cycled for five cycles at each current density from 40 to 80 mA cm⁻² under identical protocols. As shown in Figure 3, the charge and discharge capacities were recorded over five cycles at each current density. In both cells using fresh



electrolytes, the first charge cycle yielded the highest capacity. At a given current density, charge capacity exceeded discharge capacity, consistent with $CE < 100\%$. With CHA, both charge and discharge capacities decreased as the current density increased and remained stable over the five cycles at each set point (Figure 3b). Without the additive, the charge capacity was higher overall and decreased with increasing current density, whereas the discharge capacity varied less with current, resulting in comparatively larger energy loss than in the CHA-containing cell, due to the wider difference between the charge and discharge capacities (Figure 3a).

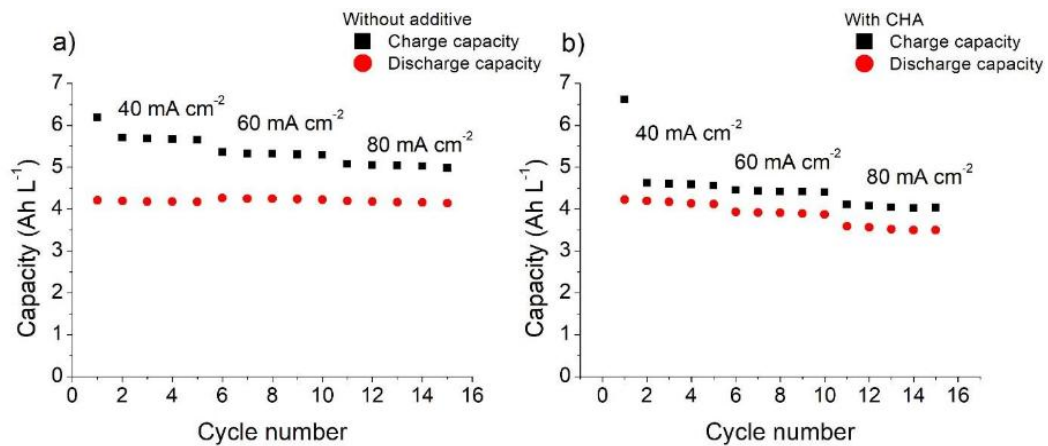


Figure 3. Charge and discharge capacities versus cycle number for AQBFs (a) without additive and (b) with CHA, cycled five times at each current density (40–80 mA cm⁻²).

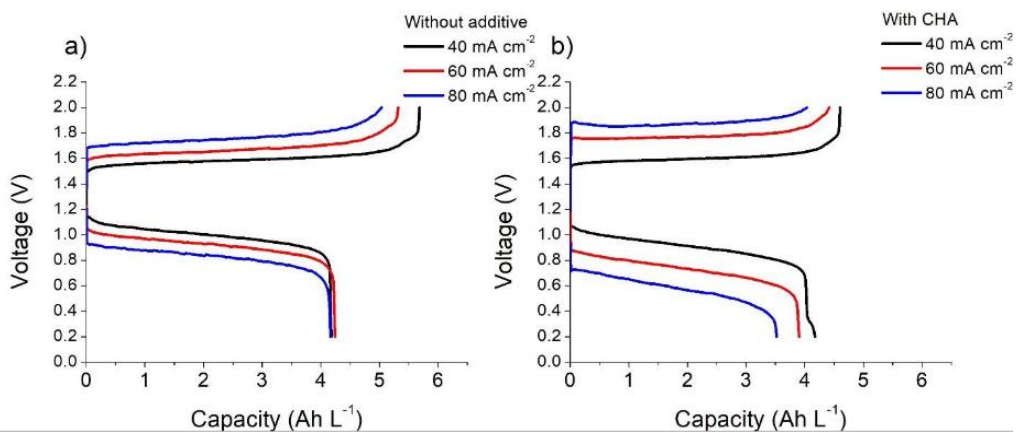


Figure 4. Voltage–capacity profiles for AQBFs (a) without additive and (b) with CHA at charging/discharging current densities of 40–80 mA cm⁻².

The voltage–capacity profiles in Figure 4 show increasing polarization (higher charge and lower discharge potentials) as the current density increased from 40 to 80 mA cm⁻², accompanied by reduced capacities. The CHA-containing cell exhibited higher overpotentials than the additive-free control, consistent with the observed efficiency trends at elevated current densities (Figure 4b). At 40 mA cm⁻², the charge curve for the CHA cell approached the water-splitting region. In the additive-free cell, the discharge capacity at 60 mA cm⁻² exceeded that at 40 mA cm⁻², deviating from a strictly monotonic trend (Figure 4a).

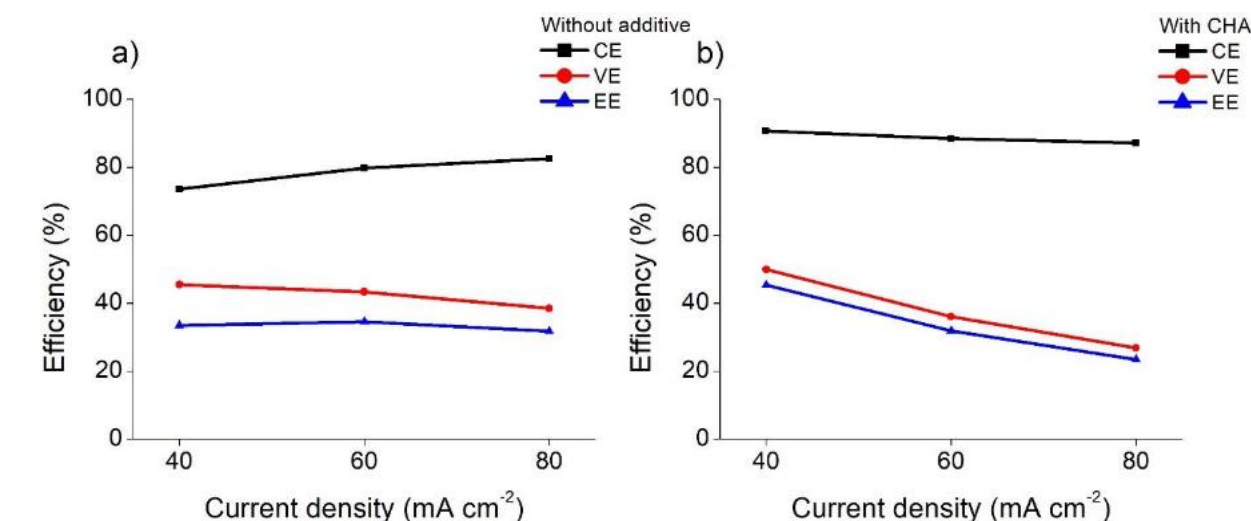


Figure 5. Coulombic, voltage, and energy efficiencies for AQBFs (a) without additive and (b) with CHA across current densities of 40–80 mA cm⁻².

The efficiency metrics in Figure 5 quantifies these behaviors. With CHA, CE reached 90.68%, 88.51%, and 87.18% at 40, 60, and 80 mA cm⁻², respectively, exceeding the additive-free control (73.56%, 79.75%, and 82.63%). The voltage efficiency (VE) decreased with current density for both cells. At 40 mA cm⁻², VE and energy efficiency (EE) were 49.98% and 45.32% with CHA versus 45.49% and 33.47% without additive. At 60 and 80 mA cm⁻², both VE and EE for the CHA cell were lower than those of the control, indicating a current-dependent efficiency trade-off.

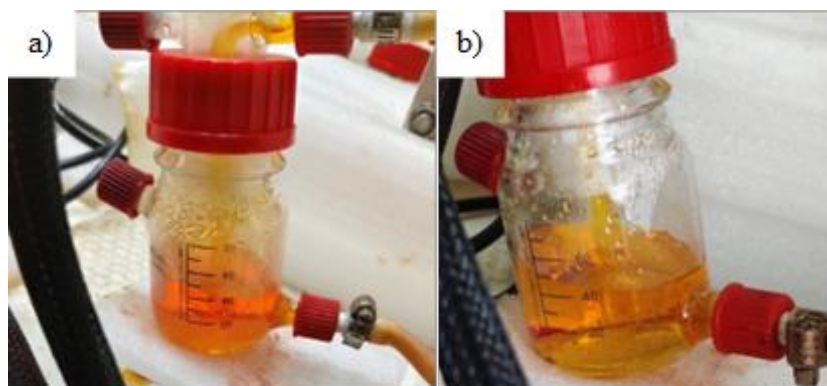


Figure 6. Appearance of the catholytes (a) without additive and (b) with CHA after testing.

After testing as shown in Figure 6, observations of catholytes showed a faint light-yellow vapor upper catholyte in the additive-free cell (Figure 6a). In contrast, the CHA-containing cell showed a minor oil phase and did not exhibit a faint light-yellow vapor (Figure 6b).

Discussion

Across current densities, the AQFBF containing CHA exhibited more stable cycling behavior, whereas both charge and discharge capacities decreased with increasing current density (Figure 3b). This trend is consistent with electrochemical systems in which higher applied currents intensify polarization and internal resistive losses, thus constraining accessible capacity [12]. By contrast, the additive-free cell deviated from a strictly monotonic discharge-capacity trend: charge capacity decreased with current density, but discharge capacity varied less and, in one case, exceeded the lower-current value (Figure 3a). A plausible interpretation is that, without a complexant, rapid formation of free Br_2 at the cathode elevates apparent charge capacity, while the high vapor pressure and reactivity of Br_2 promote active-species loss and parasitic processes that depress discharge capacity and increase energy loss [13]. Enhanced halogen mobility and transport at higher currents may further modify local speciation and utilization, contributing to the observed non-monotonicity [14].

Voltage–capacity profiles corroborate these behaviors (Figure 4). Polarization increased with current density in both cells, and the CHA-containing cell showed higher overpotentials, in agreement with

the efficiency penalties at elevated currents (Figure 5). This is consistent with the formation of larger CHA-Br_n associates that alter transport and kinetics relative to the additive-free electrolyte [11].

Efficiency metrics summarize the trade-space (Figure 5). With CHA, CE was higher at all currents, indicating reduced active-species loss during cycling, whereas VE (and therefore EE) declined more steeply at $60\text{--}80\text{ mA cm}^{-2}$, reflecting increased polarization at higher rates. Post-test observations of catholytes support these interpretations: the additive-free cell exhibited a faint light-yellow vapor upper catholyte, consistent with headspace loss of volatile, whereas the CHA-containing cell showed only a minor oil phase (Figure 6). Taken together, Figures 3-5 indicate that CHA improves coulombic efficiency and cycling stability by shifting bromine speciation toward bound polybromides, while introducing a current-dependent penalty in VE/EE that becomes more pronounced at higher rates.

Conclusions

We evaluated AQBFb incorporating 3-chloro-2-hydroxypropyltrimethylammonium chloride (CHA) as an aqueous bromine-complexing additive across $40\text{--}80\text{ mA cm}^{-2}$. Relative to the additive-free electrolyte, the CHA formulation delivered higher CE at all tested rates, reaching 90.68% at 40 mA cm^{-2} , and exhibited stable charge-discharge cycling. As current density increased, VE and, consequently, energy EE declined more steeply in the CHA cell, indicating a current-dependent polarization penalty.

The efficiency trends are consistent with bromine speciation shifted toward bound polybromides and CHA-Br_n associates. The CHA additive stabilizes bromides and polybromides in complexants, which mitigate free Br_2 and reduce active-species loss, thereby leading to an increase in CE. However, this process also introduces transport/kinetic limitations that depress VE/EE at higher rates. Post-test observation of the catholyte, which had only a minor oil phase and did not exhibit a faint light-yellow vapor, further supports reduced volatility and improved day-to-day operability with CHA. The hydroxylated, quaternary-ammonium structure of CHA provides aqueous miscibility, limiting phase separation compared with oil-phase complexants.



Overall, CHA emerges as a practical, low-cost, fully aqueous complexant for AQBFBs when high CE and improved operability are prioritized, with the trade-off of lower VE/EE at elevated current densities. These results delineate a clear operating window for CHA-enabled AQBFBs and support its consideration in systems targeting reliable, scalable, and lower-maintenance grid-level storage.

AUTHOR INFORMATION

Corresponding Author

*Corresponding Author E-mail: Soorathep.K@chula.ac.th

Present Addresses

¹Department of Chemical Engineering, Faculty of Engineering, Chulalongkorn University, Bangkok 10330, Thailand

²Department of Chemical Technology, Faculty of Science, Chulalongkorn University, Bangkok 10330, Thailand

Author Contributions

Conceptualization: P. A., P. T. and S. K.

Methodology: P. A., P. T. and S. K.

Experiments: P. A.

Formal analysis: P. A., P. T., M. S. and S. K.

Funding acquisition: S. K.

Supervision: M. S. and S. K.

Writing – original draft: P. A.

Writing – review and editing: S. K.



ACKNOWLEDGMENT

We are very much grateful to all the authors for their contributions to this exciting issue. Thanks to Department of Chemical Engineering, Faculty of Engineering of Chulalongkorn University for providing the resources and facilities necessary for conducting this research.

1. Ould Amrouche, S., Rekioua, D., Rekioua, T. & Bacha, S. Overview of energy storage in renewable energy systems. *International Journal of Hydrogen Energy* **41**, 20914-20927 (2016).
2. Wang, W., Lu, Y.-C., Wang, Q. & Li, X. Aqueous Flow Batteries for Energy Storage. *Energy Material Advances* **5**, 0133
3. Krishnamurti, V. *et al.* Aqueous organic flow batteries for sustainable energy storage. *Current Opinion in Electrochemistry* **35**, 101100 (2022).
4. Huskinson, B. *et al.* A metal-free organic–inorganic aqueous flow battery. *Nature* **505**, 195-198 (2014).
5. Petrov, M. M. *et al.* Tuning the composition of mixed anthraquinone derivatives towards an affordable flow battery negolyte. *Journal of Electroanalytical Chemistry* **973**, 118693 (2024).
6. Kerr, E. F. *et al.* High Energy Density Aqueous Flow Battery Utilizing Extremely Stable, Branching-Induced High-Solubility Anthraquinone near Neutral pH. *ACS Energy Letters* **8**, 600-607 (2023).
7. Hu, B., Luo, J., Hu, M., Yuan, B. & Liu, T. L. A pH-Neutral, Metal-Free Aqueous Organic Redox Flow Battery Employing an Ammonium Anthraquinone Anolyte. *Angewandte Chemie International Edition* **58**, 16629-16636 (2019).
8. Tang, L., Lu, W. & Li, X. Electrolytes for bromine-based flow batteries: Challenges, strategies, and prospects. *Energy Storage Materials* **70**, 103532 (2024).



9. Tang, L., Lu, W., Zhang, H. & Li, X. Progress and Perspective of the Cathode Materials towards Bromine-Based Flow Batteries. *Energy Material Advances* **2022**
10. Tang, L., Li, T., Lu, W. & Li, X. Reversible solid bromine complexation into Ti₃C₂T_x MXene carriers: a highly active electrode for bromine-based flow batteries with ultralow self-discharge. *Energy & Environmental Science* **17**, 3136-3145 (2024).
11. Li, X., Xie, C., Li, T., Zhang, Y. & Li, X. Low-Cost Titanium–Bromine Flow Battery with Ultrahigh Cycle Stability for Grid-Scale Energy Storage. *Advanced Materials* **32**, 2005036 (2020).
12. Chen, Q., Eisenach, L. & Aziz, M. J. Cycling Analysis of a Quinone-Bromide Redox Flow Battery. *Journal of The Electrochemical Society* **163**, A5057 (2016).
13. Zarei-Jelyani, M., Loghavi, M. M., Babaiee, M. & Eqra, R. The significance of charge and discharge current densities in the performance of vanadium redox flow battery. *Electrochimica Acta* **443**, 141922 (2023).
14. Wang, X. *et al.* The Impact of Wide Discharge C-Rates on the Voltage Plateau Performance of Cylindrical Ternary Lithium-Ion Batteries. *Energies* **17** (2024).



Bio-Based Quasi Solid Polymer Electrolytes for High Performance Zinc-Ion Batteries

Zia Ur Rehman¹, Peerawat Prathumrat², Nattapon Tanalue³, Chutiwat Likitaporn²,

Manunya Okhawilai^{1,2,*}, Panita Insang², Pranut Potiyaraj^{4,*}

¹*Nanoscience and Technology, Graduate School of Chulalongkorn University, Bangkok, 10330, Thailand*

²*Department of Chemical Engineering, Faculty of Engineering, Chulalongkorn University, Bangkok, 10330, Thailand*

³*Multidisciplinary Program in Petrochemistry and Polymer Science, Faculty of Science, Chulalongkorn University, Bangkok, 10330, Thailand.*

⁴*Department of Materials Science, Faculty of Science, Chulalongkorn University, Bangkok, 10330, Thailand*

*Corresponding Authors' E-mails: Manunya.O@chula.ac.th , Pranut.P@chula.ac.th

ABSTRACT

The growing demand for efficient and sustainable energy storage systems has intensified the search for green alternatives to conventional technologies. Among them, zinc-ion batteries (ZIBs) have emerged as viable options due to their low cost, high safety, natural abundance, and excellent electrochemical characteristics. In this work, we report the fabrication of bio-based quasi-solid polymer electrolyte (QSPE) based on kappa carrageenan and konjac glucomannan blended at the ratios of 100/0, 75/25, and 0/100. Among the prepared samples, the 75/25 blend showed the highest ionic conductivity of 9.93×10^{-4} S cm^{-1} and zinc ion transferring number 0.50, ensuring efficient ion transport. Zn||Zn symmetrical cell employing this electrolyte indicated cycling stability over 100 hours, highlighting its potential for long-term performance. Thermal analysis revealed melting and degradation temperatures in the ranges of 85 to 110°C and 102 to 205°C, respectively, confirming strong thermal stability for practical operation. In addition, the QSPE samples demonstrate high electrolyte uptakes and low contact angles, reflecting excellent hydrophilicity and enhanced ionic transport pathways. Overall, this bio-based QSPE design successfully integrates sustainability with electrochemical performance, offering a scalable and eco-conscious strategy for developing next-generation green ZIBs with reliable and safe energy storage capabilities.

Keywords: Bio-based polymers; Energy storage; Zinc-ion batteries; Ionic conductivity

Introduction

The growing demand for safe and sustainable energy storage in everyday applications, such as portable electronics, electric vehicles, and grid applications, has highlighted the limitations of lithium-ion batteries (LIBs). While LIBs dominate the market due to their high energy density and long cycle life, their reliance on scarce Li reserves, high production costs, and flammable organic electrolytes raises concerns over safety and sustainability. These drawbacks make LIBs less suitable for future applications that require environmentally friendly and intrinsically safe systems.

Rechargeable zinc-ion batteries (ZIBs) have emerged as a promising alternative, offering abundant zinc resources, high theoretical capacity of 820 mAh g^{-1} , sufficient redox potential of -0.76 V , and intrinsic safety of non-flammable aqueous electrolytes¹. Moreover, incorporating biodegradable and renewable materials, such as bio-based polymer electrolytes and sustainable electrodes, improves the environmental friendliness of ZIBs, aligning with the requirement for greener energy storage. However, several challenges limit the performance of ZIBs. Aqueous electrolytes, though low-cost and safe, typically suffer from low coulombic efficiency and short cycle life due to cathode dissolution and side reactions. Organic and ionic liquid electrolytes improve stability but reduce safety, cost, and sustainability. Solid-state electrolytes can address leakage issues but typically exhibit poor ionic conductivity and high interfacial resistance, while uncontrolled dendrite growth during cycling poses additional safety concerns.

To overcome these issues, quasi-solid polymer electrolytes (QSPEs) have been developed, combining the high ionic conductivity of liquid electrolytes with the mechanical strength of polymers^{2,3}. By suppressing dendrite growth, reducing side reactions, and eliminating leakage, QSPEs present a strong pathway toward reliable ZIBs. Polymer blending further enhances QSPE performance by tailoring mechanical strength, flexibility, and amorphous content for efficient ion transport^{4,5}. Yang et al.⁶ fabricated a QSPE with selective ion transport channels by crosslinking sodium polyacrylate, lithium magnesium silicate, and cellulose nanofiber, enabling Zn anodes to achieve 99.7% coulombic efficiency over 2400 cycles. Chiaoprakobkij et al.⁷ reported a konjac glucomannan (KGM)-based biopolymer electrolyte combined



with banana powder, achieving an ionic conductivity of $5.59 \times 10^{-4} \text{ S cm}^{-1}$ and stable cycling. Huang et al.⁸ designed a kappa-carrageenan (KC) electrolyte for rechargeable quasi-solid-state ZIBs, attaining excellent electrochemical performance with energy and power densities of 400 Wh kg^{-1} and 7.9 kW kg^{-1} .

Here, we report on the development of bio-based QSPEs by blending KC with KGM. Based on previous studies, KC has demonstrated the ability to enhance zinc-ion batteries with excellent electrochemical performance, achieving high energy and power densities by facilitating efficient ion transport pathways. Meanwhile, KGM has been employed as a host polymer in biopolymer electrolytes, exhibiting a notable ionic conductivity and stable cycling performance, attributed to its strong film-forming and stabilizing properties. KC, a sulfated polysaccharide derived from red seaweeds, provides strong gel-forming ability and abundant hydroxyl/sulfate groups that facilitate Zn^{2+} coordination^{9,10}. KGM, a water-soluble dietary fiber extracted from *Amorphophallus konjac*, contributes to excellent film-forming, thickening, and stabilizing capabilities¹¹. The combination of KC and KGM resulted in a QSPE with balanced ionic conductivity, mechanical strength, and structural integrity. This design addresses the conductivity-stability trade-off and advances the use of renewable, biodegradable polymers in next-generation ZIBs.

Experimental

1. Materials

Konjac glucomannan (KGM, $\geq 90\%$ purity) was supplied from Ap Operations Co., Ltd, Thailand. Kappa carrageenan (KC, 100% purity) was obtained by Bangkok Chemical Co., Ltd, Thailand. Zinc sulfate (ZnSO_4) was purchased from Sigma-Aldrich. Glycerol as a plasticizer was purchased from Kemaus.

2. Electrolyte Synthesis

The preparation process of QSPE is displayed in Figure 1. The QSPE was synthesized via a simple, cost-effective solution casting method. Initially, KC and KGM solutions with concentrations of 1 and 1.5 wt% were prepared by dissolving in 100 mL of deionized (DI) water, followed by the addition of 1 g of glycerol

as a plasticizer. The mixture was stirred for 2 hours at 85 °C at 200 rpm until a homogeneous solution was obtained. Subsequently, a 1 mL of a 2 M ZnSO₄ solution was added while stirring. Salt incorporation was considered complete when the solution became optically clear without visible undissolved particles. The resulting blend was cast into a Teflon mold and dried at 50 °C to form electrolyte films with a typical size of approximately 10 × 8 cm² and a thickness of 150 μm. Three samples with varying KC:KGM ratios of 100:0, 75:25, and 0:100 were prepared for further investigation.

3. Coin Cell Assembly

For the electrochemical evaluation, zinc symmetrical cells were fabricated using CR2032-type coin cells as shown in Figure 1. Zinc foils served as electrodes, sandwiching the prepared QSPE membrane. Before assembly, the membrane was immersed in 2 M ZnSO₄ for 10 minutes to enhance ionic conductivity, and an additional 10 μL of the same electrolyte was dropped onto the QSPE. A stainless steel spacer and spring were then placed to ensure stable contact and uniform pressure. The sealed coin cells were subsequently subjected to electrochemical testing.

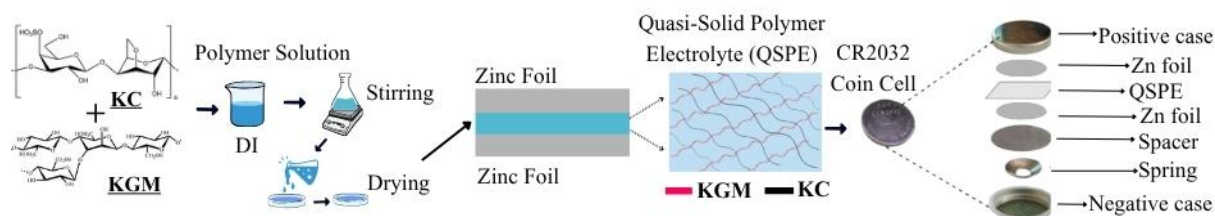


Figure 1. The preparation process of QSPE and coin cell assembly

4. Characterization Techniques

The thermal properties of the samples were analyzed by differential scanning calorimetry (DSC1 module, Mettler-Toledo). The samples were tested in a temperature range of 25 to 200 °C with a heating rate of 10°C min⁻¹ under nitrogen atmosphere. Thermogravimetric analysis (TGA, model TGA1 Module, Mettler-Toledo) to explore the phase transition and thermal stability of the samples. The analysis was performed in a temperature range of 25 to 800 °C with a heating rate of 10°C min⁻¹ under nitrogen atmosphere. These



data, including melting and degradation temperatures, are critical to confirm the electrolyte stability under battery operation conditions.

To evaluate the mechanical properties of the QSPE samples, the tensile stress-strain tests were performed using a universal testing machine (Instron 5567, USA). The tests were carried out regarding ASTM D882 standard.

Surface wettability was studied by water contact angles using an optical contact angle instrument. The water drop was captured using a camera at the first second. The electrolyte uptake of the samples was examined by immersing the samples in a 2 M ZnSO₄ solution for 24 hrs at room temperature. The electrolyte uptake percentage was calculated as:

$$\text{Electrolyte Uptake (\%)} = \frac{W_{\text{wet}} - W_{\text{dry}}}{W_{\text{dry}}} \times 100 \quad (1)$$

Where W_{dry} is the weight of a sample before immersion (g) and W_{wet} is the weight of a sample after immersion for 24 hrs (g).

Electrochemical performance was evaluated by electrochemical impedance spectroscopy (EIS) and chronoamperometry using a potentiostat, PalmSens4 (The Netherlands). These techniques were employed to evaluate the ionic conductivity and ion transference number of the electrolyte. The ionic conductivity (σ) (S cm⁻¹) was calculated as:

$$\sigma = \frac{d}{AR} \quad (2)$$

Where d is the thickness of the sample (cm), A is the contact area (cm²), and R is the resistance of the membrane (Ω).

The ion transference number was determined by:

$$\text{Ion transference Number} = \frac{I_i - I_f}{I_i} \quad (3)$$



Where I_i is an initial current and I_f is a final current (μA).

Long-term plating/stripping tests of the Zn||Zn symmetric cells were performed using a Neware battery testing system (Shenzhen Neware CT-4008) to measure the cycling stability using a current density of 0.25 mA cm^{-2} . The duration and voltage cutoff were set at 1 hour and 5 V.

Results and Discussion

The image of KC:KGM with a 75:25 ratio is shown in Figure 2a. The mechanical properties of the KC:KGM samples with 100:0, 75:25, and 0:100 are indicated in Figure 2b. The results showed that the combination of KC:KGM at 75:25 ratio provided the highest tensile strength at approximately 10 MPa when compared with neat KC and KGM. This combination offered a more balanced and synergistic intermolecular-bonded network between KC and KGM, which led to better chain packing and load transfer efficiency. This optimized intermolecular interaction resulted in a stronger network structure, therefore giving higher tensile strength than neat KC or neat KGM.

The thermal stability of samples was investigated by TGA, as shown in Figure 2c. An initial weight loss between 30-100 °C was attributed to moisture release, reflecting the strong water affinity of polysaccharides¹². The major weight loss occurred at 230-300 °C, corresponding to the cleavage of saccharide rings and carrageenan and konjac backbones^{13,14}. Notably, the KC:KGM 75:25 blend exhibited improved thermal stability, suggesting that intermolecular interactions and improved structural compactness conferred higher resistance to degradation.

DSC thermograms, as displayed in Figure 2d, indicated endothermic peaks at 60-120 °C, associated with the loss of crystalline water entrapped during the drying process¹⁵. The KC:KGM 75:25 blend showed a significant reduction in melting enthalpy, revealing increased amorphous content and decreased crystallinity¹⁶. This transition is particularly beneficial, as greater amorphous character typically facilitates ion transport. Overall, the observed thermal behavior indicated that blending KC with KGM enhanced

thermal resistance and promoted structural features suitable for ionic conductivity and electrochemical performance in battery applications.

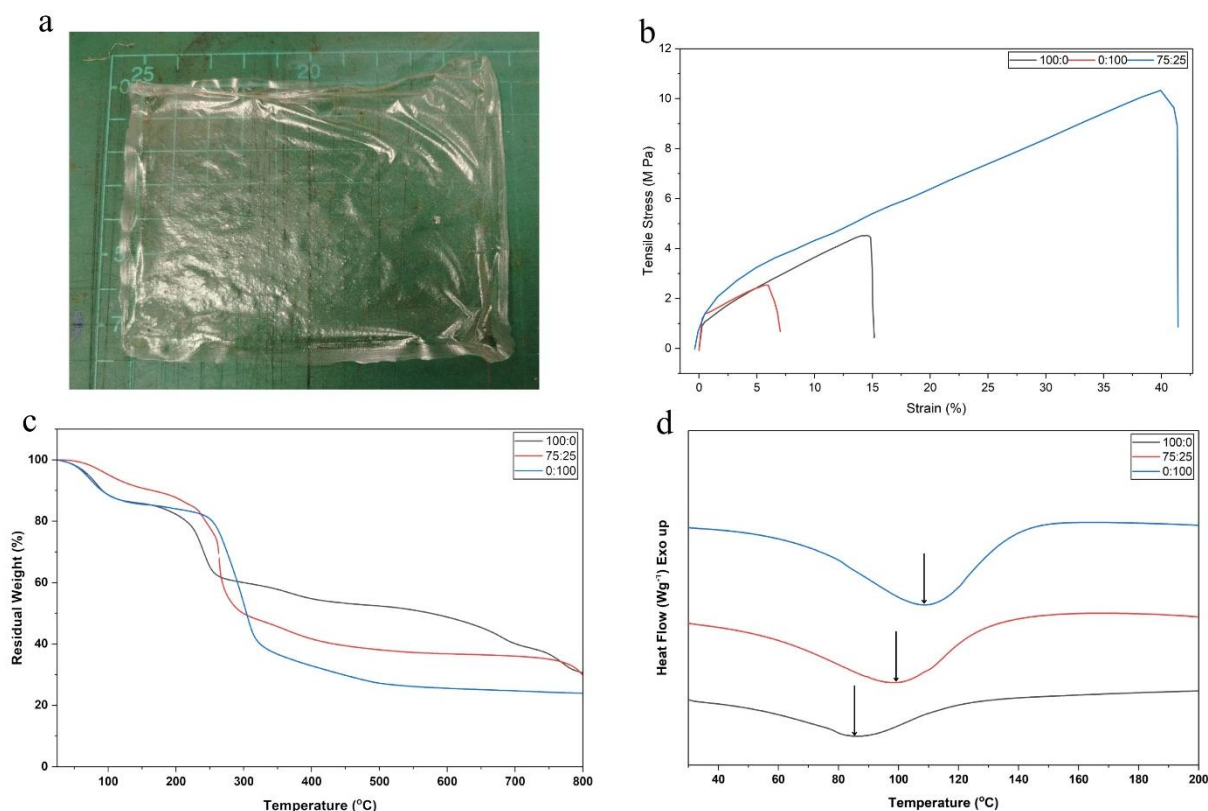


Figure 2. (a) Image of 75:35 KC:KGM electrolyte film (b) Stress strain results of samples (c) TGA and (d) DSC thermograms of QSPEs with different ratios of KC:KGM at 100:0, 75:25, and 0:100.

The wettability of the QSPEs revealed contact angles of 46°, 43°, and 29° for KC:KGM at 100:0, 75:25, and 0:100, respectively, as shown in Figure 3a. All samples showed hydrophilic surfaces, whose contact angles were less than 90°, with lower values corresponding to strong affinity for water and improved electrolyte uptake¹⁷. Electrolyte uptake results, as included in Table 1, demonstrated that the KC:KGM 100:0 had the highest uptake of 244%, which favored ionic conductivity but may reduce mechanical stability due to excessive swelling. In contrast, the KC:KGM 0:100 absorbed at least 112%, offering better stability but limited ion transport. The KC:KGM 75:25 blend achieved a balanced uptake of 203%, indicating an optimal balance between ionic conductivity and structural integrity¹⁸.



Impedance measurement, as depicted in Figure 3b, confirmed this trend, with the KC:KGM 75:25 blend showing the highest ionic conductivity of $9.93 \times 10^{-4} \text{ S cm}^{-1}$. However, the KC:KGM 100:0 and KC:KGM 0:100 samples showed 8.25×10^{-4} and $8.79 \times 10^{-4} \text{ S cm}^{-1}$, respectively. Enhanced polymer chain flexibility and amorphous content in the blended sample facilitated ion migration. KC, enriched with sulfate and hydroxyl groups, promoted salt dissociation and cation transport, while KGM contributed to hydroxyl-rich chains that improved flexibility and controlled swelling. As a result, the KC:KGM 75:25 blend also exhibited an ion transference number of 0.50, as shown in Figure 3c, confirming its excellent balance of ionic conductivity, ion transport efficiency, and structural stability, making it the most promising electrolyte formulation. In addition, Table 2 summarizes the recent works to compare the ionic conductivity of the KC:KGM sample with other QSPE systems, showing that the KC:KGM with 75:25 ratio provided higher ionic conductivity.

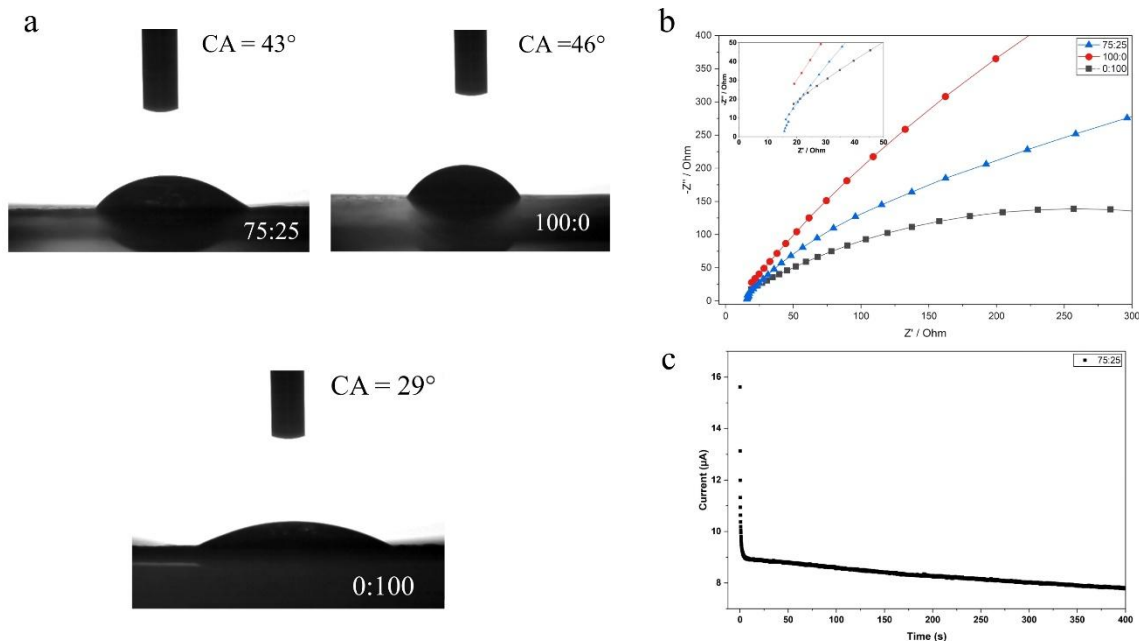


Figure 3. (a) Contact angles and (b) EIS of QSPEs with different ratios of KC:KGM at 100:0, 75:25, and 0:100, and (c) Ion transference number of the KC:KGM 75:25 blend.

Table 1. Electrolyte uptakes of KC:KGM samples.

Sample	Electrolyte Uptake (%)
100:0	244
75:25	203
0:100	112

Table 2. Ionic conductivity comparison with other polymer-based electrolytes.

Samples	Ionic Conductivity (S cm ⁻¹)	Ref
Titanium dioxide / Poly(vinyl alcohol)	1.24×10^{-5}	[20]
poly (ethylene glycol)diglycidylether	3.77×10^{-4}	[21]
poly (vinylidene fluoride-hexafluoropropylene)/ methylimidazolium trifluoromethanesulfonate	1.44×10^{-4}	[22]
KC/KGM	9.93×10^{-4}	This work

The long-term stripping/plating profiles of QSPEs assembled in symmetrical Zn||Zn cells are presented in Figure 4. Both the KC:KGM (100:0) and KC:KGM (75:25) QSPEs exhibited stable voltage profiles over 100 h, indicating good interfacial compatibility with Zn and effective suppression of dendrite growth. Notably, the KC:KGM 75:25 sample displayed a slightly higher but more stable overpotential, suggesting enhanced ion transport and enhanced interfacial stability, arising from the combined effect of KC and KGM.

On the other hand, the KC:KGM 0:100 membrane suffered from severe voltage fluctuations and rapid instability, reflecting poor interfacial compatibility and uncontrolled dendrite formation¹⁹.

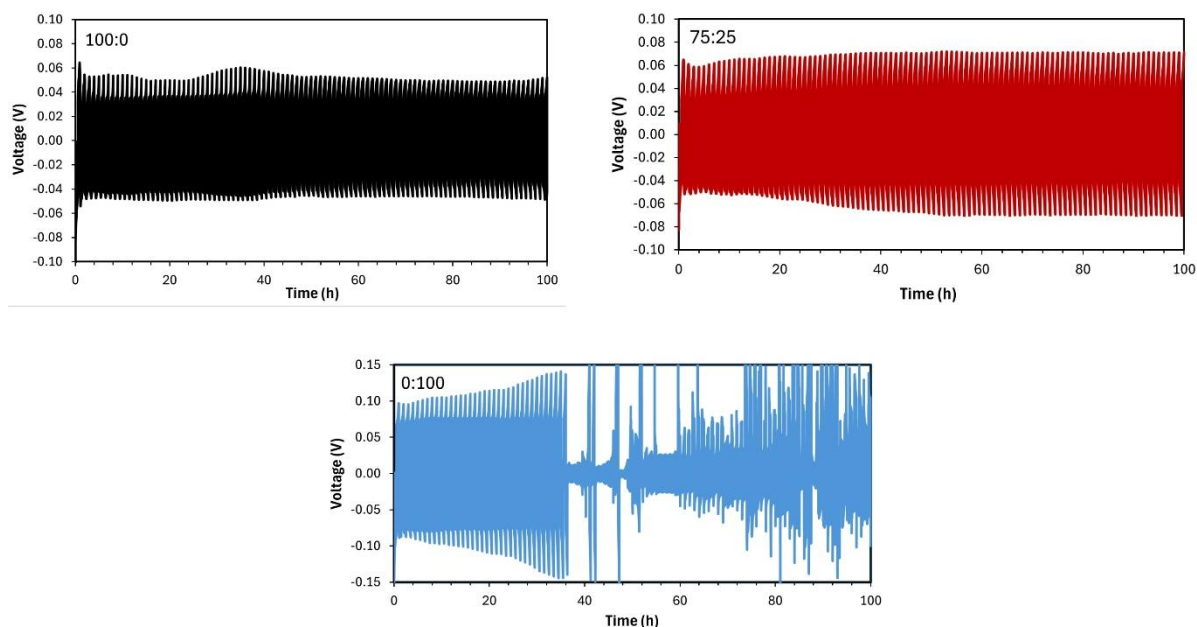


Figure 4. Long-term stripping/plating profiles of the symmetrical Zn||Zn cells at various QSPE samples with different ratios of KC:KGM at 100:0, 75:25, and 0:100 at a current density of 0.25 mA cm^{-2} .

Conclusions

In this study, bio-based QSPEs were fabricated by blending KC and KGM in different ratios for ZIBs. The KC:KGM 75:25 blend demonstrated the most balanced performance, exhibiting the highest ionic conductivity of $9.93 \times 10^{-4} \text{ S cm}^{-1}$ and a transference number of 0.50, ensuring efficient ion transport. Thermal analysis confirmed strong stability, while contact angle and electrolyte uptake studies revealed excellent hydrophilicity and electrolyte affinity. Zn||Zn symmetric cell testing further validated its cycling stability and ability to suppress dendrite growth. Overall, this work demonstrates a sustainable, effective

QSPE design that integrates environmental friendliness with high electrochemical performance, advancing the development of next-generation green ZIBs.

Author Contributions

The manuscript was written through contributions of all authors. All authors have given approval to the final version of the manuscript.

Acknowledgement

The authors gratefully acknowledge financial support from the Program Management Unit for Human Resources & Institutional Development, Research and Innovation (B49G680121), the Second Century Fund (C2F), Chulalongkorn University, and the National Research Council of Thailand (NRCT) together with Chulalongkorn University (N42A680292). The funding support from Chula Engineering's promoting research grant is also acknowledged.

References

- 1 Ebraheam A-Z & Fan X. Effect of aqueous electrolyte concentration and valency on contact angle on flat glass surfaces and inside capillary glass tubes. *Colloids Surf. A.* **543**, 1-8 (2018).
- 2 Arockia Mary I, Selvanayagam S, Selvasekarapandian S, Chitra R, Leena Chandra M & Ponraj T. Lithium ion conducting biopolymer membrane based on K-carrageenan with LiNO₃. *Ionics* **26**, 4311-4326 (2020).
- 3 Bhatia S, Abbas Shah Y, Al-Harrasi A, Jawad M, Koca E & Aydemir LY. Enhancing tensile strength, thermal stability, and antioxidant characteristics of transparent kappa carrageenan films using grapefruit essential oil for food packaging applications. *ACS Omega* **9**, 9003-9012 (2024).



- 4 Callegari D, Davino S, Mustarelli P & Quartarone E. Quasi-solid polymer electrolyte with autonomous self-healing capabilities for lithium metal batteries. *J. Power Sources* **649**, 237477 (2025).
- 5 Chiaoprakobkij N, Okhawilai M, Kasemsiri P & Uyama H. Biopolymer electrolyte from banana powder-konjac glucomannan for zinc-ion batteries. *Int. J. Biol. Macromol.* **273**, 133204 (2024).
- 6 Delgado Rosero MI, Jurado Meneses NM & Uribe Kaffure R. Thermal properties of composite polymer electrolytes poly (ethylene oxide)/sodium trifluoroacetate/aluminum oxide (PEO) 10CF₃COONa+ x wt.% Al₂O₃. *Materials* **12**, 1464 (2019).
- 7 Geng X, Zhao N, Song X, Wu J, Zhu Q, Wu T, Chen H & Zhang M. Fabrication and characterization of konjac glucomannan/oat β -glucan composite hydrogel: microstructure, physicochemical properties and gelation mechanism studies. *Molecules* **27**, 8494 (2022).
- 8 Han Q, Wang H, Zhou T, Wang Y, Shen Z, Yu D, Liu X, Liu W & Lv W. Ultrastable emulsion stabilized by the konjac glucomannan-xanthan gum complex. *ACS Omega* **8**, 31344-31352 (2023).
- 9 Huang Y, Liu J, Zhang J, Jin S, Jiang Y, Zhang S, Li Z, Zhi C, Du G & Zhou H. Flexible quasi-solid-state zinc ion batteries enabled by highly conductive carrageenan bio-polymer electrolyte. *RSC Adv.* **9**, 16313-16319 (2019).
- 10 Lin W, Zheng X, Ma S, Ji K, Wang C & Chen M. Quasi-solid polymer electrolyte with multiple lithium-ion transport pathways by in situ thermal-initiating polymerization. *ACS Appl. Mater. Interfaces* **15**, 8128-8137 (2023).
- 11 Lu J, Jaumaux P, Wang T, Wang C & Wang G. Recent progress in quasi-solid and solid polymer electrolytes for multivalent metal-ion batteries. *J. Mater. Chem. A* **9**, 24175-24194 (2021).
- 12 Sangeetha P, Selvakumari T, Selvasekarapandian S, Srikumar S, Manjuladevi R & Mahalakshmi M. Preparation and characterization of biopolymer K-carrageenan with MgCl₂ and its application to electrochemical devices. *Ionics* **26**, 233-244 (2020).
- 13 Vineeth S, Soni CB, Sanjaykumar C, Yamauchi Y, Han M & Kumar V. A quasi-solid state polymer electrolyte for high-rate and long-life sodium-metal batteries. *J. Energy Storage* **73**, 108780 (2023).



- 14 Wang H,Zhang Z,Li Y,Zhang F,Yang K & Xue B. A Clay-Based Quasi-Solid-State electrolyte with high cation selective channels for High-Performance aqueous Zinc-Ion batteries. *Chem. Eng. J.* **500**, 156514 (2024).
- 15 Wardhana YW,Aanisah N,Sopyan I,Hendriani R & Chaerunisaa AY. Gelling power alteration on kappa-carrageenan dispersion through esterification method with different fatty acid saturation. *Gels* **8**, 752 (2022).
- 16 Wongsalam T,Okhawilai M,Kheawhom S,Qin J,Kasemsiri P,Likitaporn C & Tanalue N. Highly efficient suppression of zincate ion crossover in zinc–air batteries using selective membrane PVA-KOH/ZIF-8 gel polymer electrolytes. *J. Energy Storage* **89**, 111773 (2024).
- 17 Xu X,Li B,Kennedy JF,Xie BJ & Huang M. Characterization of konjac glucomannan–gellan gum blend films and their suitability for release of nisin incorporated therein. *Carbohydr. Polym.* **70**, 192-197 (2007).
- 18 Yang C,Woottapanit P,Geng S,Chanajaree R,Shen Y,Lolupiman K,Limphirat W,Pakornchote T,Bovornratanaraks T & Zhang X. A multifunctional quasi-solid-state polymer electrolyte with highly selective ion highways for practical zinc ion batteries. *Nat. Commun.* **16**, 183 (2025).
- 19 Zakaria Z,Kamarudin SK,Osman SH,Mohamad AA & Razali H. A review of carrageenan as a polymer electrolyte in energy resource applications. *J. Polym. Environ.* **31**, 4127-4142 (2023).
- 20 Liu C,Tian Y,An Y,Yang Q,Xiong S,Feng J & Qian Y. Robust and flexible polymer/MXene-derived two dimensional TiO₂ hybrid gel electrolyte for dendrite-free solid-state zinc-ion batteries. *Chem. Eng. J.* **430**, 132748 (2022).
- 21 Dong H,Li J,Zhao S,Zhao F,Xiong S,Brett DJ,He G & Parkin IP. An anti-aging polymer electrolyte for flexible rechargeable zinc-ion batteries. *J. Mater. Chem. A* **8**, 22637-22644 (2020).
- 22 Liu J,Ahmed S,Khanam Z,Wang T & Song S. Ionic liquid-incorporated zn-ion conducting polymer electrolyte membranes. *Polymers* **12**, 1755 (2020).



dreamstime.



<https://www.thaienergystorage.org/power-to-x-for-a-sustainable-future-work>